NUMERICAL METHODS FOR STUDYING SELF-SIMILAR PROPAGATION OF VISCOUS GRAVITY CURRENTS

A Thesis

Submitted to the Faculty

of

Purdue University

by

Aditya Avinash Ghodgaonkar

In Partial Fulfillment of the

Requirements for the Degree

of

Master of Science in Mechanical Engineering

May 2019

Purdue University

West Lafayette, Indiana

THE PURDUE UNIVERSITY GRADUATE SCHOOL
STATEMENT OF THESIS APPROVAL

Dr. Ivan C. Christov, Chair

School of Mechanical Engineering

Dr. Arezoo Ardekani

School of Mechanical Engineering

Dr. Osman Basaran

School of Chemical Engineering

Approved by:

Dr. Jay P. Gore

Head of the Graduate Program

ACKNOWLEDGMENTS

First and foremost, I would like to express my sincere gratitude to my advisor, Prof. Ivan Christov, whose invaluable guidance and mentoring has helped me immensely in the completion of this master's research and beyond. I would also like to thank my committee members, Profs. Arezoo Ardekani and Osman Basaran for their advice and questions. I have greatly enjoyed the opportunity to work with my lab-mates at the TMNT Lab; their comments and feedback in the preparation of the defense of thesis is greatly appreciated. The bulk of this work has been submitted for publication as a chapter entitled "Solving Nonlinear Parabolic Equations by a Strongly Implicit Finite-Difference Scheme: Applications to the Finite-Speed Spreading of Non-Newtonian Viscous Gravity Currents" in the Springer edited volume *Advanced Wave Mathematics II* (preprint arXiv:1903.07568); I would like to thank Profs. Tarmo Soomere and Arkadi Berezovski for their efforts in editing this volume and their kind invitation to contribute a chapter. I would like to extend my gratitude to Dr. Zhong Zheng in his experimental data on second-kind self-similarity, which has complemented the discussion on the numerical approach proposed in this thesis. I also appreciate Prof. Sandro Longo's contribution of the idea of extending the discussion of second-kind self-similarity to non-Newtonian fluids. Finally, I would like to express heartfelt gratitude to my family and friends. Their constant support and encouragement have been key to the successful completion of this master's research.

TABLE OF CONTENTS

Page

LIST OF TABLES

LIST OF FIGURES

ABSTRACT

Ghodgaonkar, Aditya Avinash M.S.M.E., Purdue University, May 2019. Numerical Methods for Studying Self-similar Propagation of Viscous Gravity Currents. Major Professor: Ivan C. Christov.

A strongly implicit, nonlinear Crank-Nicolson-based finite-difference scheme was constructed for the numerical study of the self-similar behavior of viscous gravity currents. Viscous gravity currents are low Reynolds number flow phenomena in which a dense, viscous fluid displaces a lighter (usually immiscible) fluid. Under the lubrication approximation, the mathematical description of the spreading of these fluids is reduced to solving a nonlinear parabolic partial differential equation for the shape of the fluid interface. This thesis focuses on the finite-speed propagation of a power-law non-Newtonian current in a variable width channel-like geometry (a "Hele-Shaw cell") subject to a given mass conservation/balance constraint. The proposed numerical scheme was implemented on a uniform but staggered grid. It is shown to be strongly stable, while possessing formal truncation error that is of second-order in space and it time. The accuracy of the scheme was verified by benchmarking it against established analytical solutions, which were obtained via a first-kind self-similarity transformation. A series of numerical simulations confirmed that the proposed scheme accurately respects the mass conservation/balance constraint. Next, the numerical scheme was used to study the second-kind self-similar behaviour of Newtonian viscous gravity currents flowing towards the end of a converging channel. Second-kind self-similar transformations are not fully specified without further information from simulation or experiment. Thus, using the proposed numerical scheme, the self-similar spreading and leveling leveling of the current was definitively addressed. The numerical results showed favorable comparison with experimental data.

1. INTRODUCTION

Although most wave phenomena in classical continuum mechanics relate to a hyperbolic (wave) equation, one of the surprises of 20th century research into nonlinear partial differential equations (PDEs) is that *certain* parabolic (diffusion) equations also yield structures with finite speed of propagation. Two examples are (i) a linear diffusion equation with a nonlinear reaction term [1, 2], and (ii) a diffusion equation that is nonlinear due to a concentration-dependent diffusivity [3].[1] Indeed, it is known that certain aspects of wave phenomena can be reduced to a problem of solving a parabolic PDE, as illustrated by Engelbrecht [5, Ch. 6] through a series of selected case studies; further examples include, but are not limited to: electromagnetic waves along the earth's surface [6], seismic waves [7], underwater acoustics [8], and the classical theory of nerve pulses [5, Sec. 6.4.2], which nowadays has been updated by Engelbrecht et al. [9] to a nonlinear hyperbolic (wave) model in the spirit of the Boussinesq paradigm [10, 11].

Of special interest to discussion presented in this thesis were physical problems that are modeled by nonlinear parabolic PDEs. These nonlinear problems lack general, all-encompassing solution methodologies. Instead, finding a solution often involves methods that are specific to the nature of the governing equation or the physical problem it describes [12, Ch. 4] (see also the discussion in [13] in the context of heat conduction). The classical examples of nonlinear parabolic PDEs admitting traveling wave solutions come from heat conduction [14, Ch. X] (see also [15]) and thermoelasticity [15, 16]. The sense in which these nonlinear parabolic PDEs admit traveling-wave and 'wavefront' solutions now rests upon solid mathematical foundations [17, 18].

[1] More specifically, Barenblatt [3] (see also [4, p. 13]) credits the observation of finite-speed of propagation in nonlinear diffusion equations to a difficult-to-find 1950 paper by Zeldovich and Kompaneets.

Another classical example of a nonlinear parabolic PDE governing the finite-speed wave-like motion of a substance arises in the study of an ideal gas spreading in a uniform porous medium [3]. A similar nonlinear parabolic equation can be derived for the interface between a viscous fluid spreading horizontally underneath another fluid of lower density ($\Delta\rho > 0$ between the fluids) [19]. The motion of the denser fluid is dictated by a balance of buoyancy and viscous forces at a low Reynolds number (viscous forces dominate inertial forces). Such viscous gravity current flows are characterized by 'slender' fluid profiles i.e., they have small aspect ratios ($H_c/L \ll 1$, where H_c and L are typical vertical and horizontal length scales). Therefore, these flows can be modeled by lubrication theory [20, Ch. 6]. A representation of the flow geometry associated with typical gravity current flow in a thin channel like geometry is shown in Figure 1.1. Generically, one obtains a nonlinear parabolic equation for the gravity current's shape h as a function of the flow-wise coordinate x and time t. The case of the spreading of a fixed mass of Newtonian fluid was originally explored contemporaneously by Didden [21] and Huppert [19].

Being governed by a parabolic (irreversible) equation, these currents 'forget' their initial conditions at intermediate times; this is Barenblatt's concept of *intermediate asymptotics* [22, 23]. It follows that a *universal* current profile can be obtained by a self-similarity transformation of the current shape $h(x,t)$, which reduces the PDE in Equation (2.1) to an ordinary differential equation (ODE). Since the similarity variable can obtained by a scaling (dimensional) analysis, this kind of solution is known as self-similarity of the *first* kind [23, Ch. 3]. Specifically, the transformation is of the form $h(x,t) = t^{\beta} f(\zeta)$, where $\zeta = x/(\eta_N t^{\delta})$ is the similarity variable, and $f(\zeta)$ is the universal shape function to be determined by solving an ODE. The exponents β and δ are obtained through scaling (dimensional analysis) of the original PDE, and η_N is a constant that ensures ζ is dimensionless. An example of how this self-similar transformation is performed is discussed in Appendix A.

First-kind self-similarity has been used to analyze the propagation of Newtonian viscous gravity current flows in a variety of physical scenarios. For example, gravity

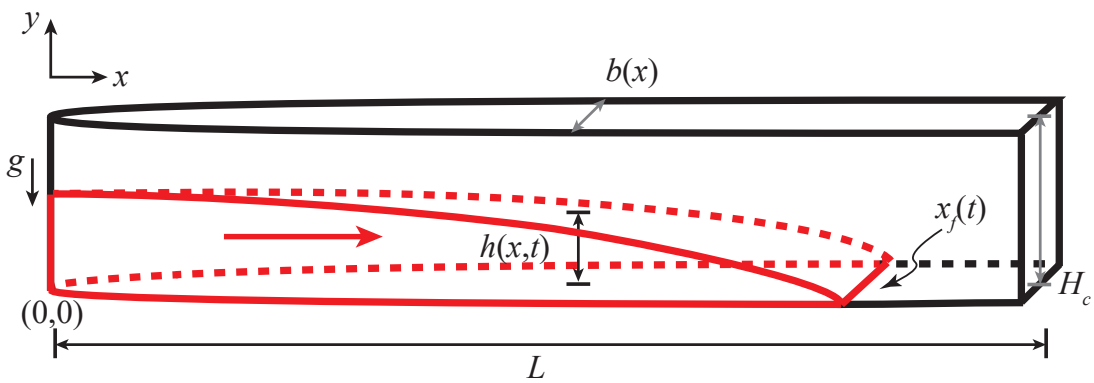

Fig. 1.1. An example schematic representation of a gravity current spreading in a thin channel-like geometry (a Hele-Shaw cell). The channel width $b(x)$ is allowed to be a function of the streamwise coordinate x. The Hele-Shaw cell has a small vertical aspect ratio: $H_c/L \ll 1$. A dense fluid flows along the bottom of the channel and displaces a much lighter fluid (assumed to be air). Typically, the current is released at an origin ($x = 0$), where the width vanishes ($b(0) = 0$) and spreads in one direction only (here, to the right). Of interest is the evolving shape of the fluid interface $h(x, t)$ and the position of the nose or 'front' of the current $x_f(t)$. Figure reproduced and adapted with permission from [Zheng et al., Influence of heterogeneity on second-kind self-similar solutions for viscous gravity currents, J. Fluid Mech., vol. 747, p. 221] © Cambridge University Press 2014.

currents arise in geophysical applications associated with flows through porous rocks [24] such as in ground water extraction [25], during oil recovery [26, 27], and during CO_2 sequestration [28]. In these examples, the current shape $h(x, t)$ represents an interface between two immiscible fluids in the limit of large Bond number (gravity dominates surface tension). There is now an extensive literature featuring a wealth of exact and approximate analytical self-similar solutions for gravity currents in porous media, e.g., [3, 29–38] among many others.

Moving beyond 'simple' fluids, one tractable model of non-Newtonian rheological response is the *power-law fluid*; this is also known as the Oswald–de Weale fluid [39]. In unidirectional flow, the power-law model simply dictates that fluid's viscosity depends upon a power of the shear rate (velocity gradient). Power-law fluid flow in

Hele-Shaw cells has been of interest; for example, Di Federico et al. [40] generalized Huppert's problem [19] to this case, although Gratton et al. [41, 42] had also considered some related problems. Even earlier, Kondic et al. [43, 44] derived the governing equations for power-law fluids in Hele-Shaw cells, under the lubrication approximation, due to the interest in studying the Saffman–Taylor instability (colloquially termed 'viscous fingering' instability) associated with injection of a less viscous fluid (typically air) into a non-Newtonian fluid. Such works have contributed to the use of a modified Darcy law to model the flow non-Newtonian flow in porous media under the Hele-Shaw analogy. Aronsson and Janfalk [45] were perhaps the first to combine an effective Darcy law for a power-law fluid with the continuity equations to obtain a single PDE, of the kind studied here, governing the gravity current's shape. Recently, Lauriola et al. [46] highlighted the versatility of this modeling approach by reviewing and extending the existing literature to two-dimensional axisymmetric currents spreading in media with uniform porosity but variable permeability. In this thesis, emphasis is placed on the propagation of non-Newtonian gravity currents, specifically ones for which the denser fluid obeys a power-law rheology. These flows are of interest because others have been exact analytical self-similar solutions in closed form [41, 47–50]. Specifically, the solution of Ciriello et al. [50] will be used in Section 4.1 below to verify the truncation error of the proposed numerical method.

For a self-similar solution to exist, both the governing PDE and its boundary conditions (BCs) must properly transform into an ODE in ζ with suitable BCs. A number of studies have specifically shown that the volume of fluid within the domain can be transient, varying as a power-law in time $\mathcal{V}(t) \propto t^{\alpha}$ ($\alpha \geq 0$) and a self-similar solution still exists (see, e.g., [3, 31, 33, 38, 48, 49] and the references therein). However, the nonlinear ODE in ζ often cannot be integrated exactly in terms of a known function, except for when $\alpha = 0$. Section 2.2 below details the manner in which a constraint of the form $\mathcal{V}(t) \propto t^{\alpha}$ can be implemented numerically through flux BCs at the computational domain's ends.

With increasing complexity of the flow physics incorporated in the model, finding a self-similarity transformation may no longer be possibly simply by using scaling (dimensional) arguments in certain cases. Gratton and Minotti [51] classified a number of such examples, including the so-called 'focusing' flows involving an axisymmetrically converging fluid flow towards the origin on a flat planar surface. A more recent study by Zheng et al. [52] extended this work to include a vertically leaky or permeable substrate over which the converging Newtonian viscous gravity current. Further examples involving confined currents in channels with variable width, and/or gravity currents in porous media whose permeability and porosity are functions of x, were proposed by Zheng et al. [38] (see, e.g., Figure 2.1). Though a self-similar transformation cannot be obtained by scaling arguments in these cases, the gravity currents nevertheless do enter a self-similar regime. This is because flows of this type involve an additional length scale, the instantaneous location front or 'nose' of the fluid as it approaches the origin. The appearance of this length scale in the global mass conservation constraint makes this a nontrivial problem from a scaling point-of-view. Now, the exponents β and δ in the transformation are unknown *a priori*. This situation represents a self-similarity of the *second* kind [23, Ch. 4]. The governing nonlinear parabolic PDE can be transformed to a nonlinear ODE, then a nonlinear eigenvalue problem must be solved for β and δ through a phase plane analysis [51, 53]. Alternatively, experiments or numerical simulations are necessary to determine β and δ. For example, early numerical simulations were performed to this end by Diez et al. [54].[2] However, a 'pre-wetting film' ahead of the current's sharp wavefront ($x = x_f(t)$ where $h\big(x_f(t), t\big) = 0$) was required to avoid numerical instabilities. The scheme therein was also first-order accurate in time only. In this this thesis an attempt was made to utilize a modern, high-order-accurate implicit numerical method to investigate the matter of second-kind self-similarity in viscous-gravity currents.

[2]See also the work of Angenent and Aronson [55], which provided a more detailed mathematical analysis of second-kind self-similarity in this flow.

Specifically, a strongly implicit numerical scheme for one-dimensional nonlinear parabolic PDEs arising in the study of gravity currents was developed and benchmarked. Efforts were made to show the utility of proposed scheme in simulating the spreading of one-dimensional *non-Newtonian* viscous gravity currents in variable geometries, and to show rigorous the sheme's high accuracy and at low computational expense. To this end, this thesis builds upon the work of Zheng et al. [38], which introduced this type of finite-difference scheme for simulating the spreading of a finite mass of Newtonian fluid in a variable-width Hele-Shaw cell. Specifically, experiments from the latter study are reconsidered in the context of second-kind self-similarity. Thus while most of the discussion of the numerical scheme development is about power-fluids, the discussion of second-kind self-similarity is limited to the case of the release of a fixed mass of Newtonian current in a completely porous HS cell of variable width. Based on established mathematical theory, numerical simulations were expected to be indicative of two distinct self-similar regimes for the case of a current spreading *towards* the closed end of the variable width Hele-Shaw cell: a 'pre-closure' regime, during which a current spreads towards the channel end; and a 'post-closure' regime, which occurs once a current reached the end of the cell and begins to leveling.

This thesis is organized as follows. In Chapter 2, briefly summarizes existing models describing certain flows of viscous gravity currents. Following this, a convenient general notation for such nonlinear parabolic PDEs is introduced. The derivation of the BCs for the PDE, from the mass conservation constraint, is discussed in Section 2.2. Then, the manner in which the nonlinear Crank–Nicolson scheme was constructed is detailed in Section 3.2 and the discretized form of the nonlinear flux BCs are discussed in Section 3.3. In Section 3.1, the one-dimensional uniform, staggered grid upon which the finite-difference scheme is implemented is introduced. Continuing, Section 4.1 reports a study of scheme's accuracy performed by comparing the numerical solution provided by the finite-difference scheme (up to a specified physical time) against an analytical solution obtained through a self-similar transformation of the PDE. Specifically, this approach involves three validation cases: (i) a symmet-

ric (about $x = 0$) lump of fixed fluid mass spreading in two directions (convergence independent of BCs), (ii) a fixed fluid mass spreading away from the origin ($x = 0$) (no fluid injection BCs), and (iii) a variable fluid mass being injected at the origin spreading away from it (required careful implementation of the full nonlinear BCs). In all three cases, the scheme can be shown to be capable of accurately computing the gravity current shape and its spreading in time. In Section 4.2, the scheme's conservation properties are analyzed by verifying numerically that it respected the mass constraint $\mathcal{V}(t) \propto t^{\alpha}$. Two validation cases are considered: (i) release of a fixed fluid mass ($\alpha = 0$), and (ii) fluid mass injection into the domain ($\alpha > 0$). In both cases, there was a specific focus on the challenging case of a non-Newtonian (power-law) displacing fluid in a variable-width channel. Thereafter, the second-kind self-similar case of a Newtonian fluid spreading towards the origin of a variable-width HS cell is studied, beginning with Section 5.2 in which the analytical self-similar transformation for second-kind self-similarity is summarized. Section 5.3 provides details and observations on a previously conducted on the release of a fixed mass of a 95% glycerol-water mixture in a shaped HS cell. Finally, numerical simulations using the proposed scheme are used in Section 5.4 to provide better insight into the onset of two distinct self-similar regimes during spreading (Section 5.4.1) and leveling (Section 5.4.2) of the gravity current. The analytical, numerical and experimental results are compared and contrasted to convincingly show the existence of second-kind self-similar behavior in this flow. Finally, for completeness, the previously derived first-kind self-similar solutions from the literature, which are used as benchmark solutions for the proposed scheme, are summarized in Appendix A.

2. PRELIMINARIES

In this chapter, the mathematical model for viscous gravity currents in a selected set of applications involving Newtonian and non-Newtonian fluids is summarized. Specifically, of interest is the spreading of a liquid in a fixed- or variable-width channel geometry (a "Hele-Shaw cell"), as well as flows in heterogeneous porous media with independently variable permeability and porosity. Ultimately it is shown that all these models can be concisely summarized by a single nonlinear parabolic PDE supplemented with a set of nonlinear Neumann (flux) BCs.

2.1 Fluid Domain and Flow Characteristics

The flow domain is assumed to be long and thin. For example, it could be a channel existing in the gap between two impermeable plates, i.e., a Hele-Shaw (HS) cell, which may or may not have variable transverse (to the flow) width as shown in Figure 2.1(a); or it could be uniformly thick slab of heterogeneously porous material, as shown in Figure 2.1(c). The viscous gravity current considered consists of one fluid displacing another immiscible fluid. Therefore, a sharp interface $y = h(x, t)$ separates the two fluids at all times. The present study considers the limit of negligible surface tension (i.e., negligible surface forces); as mentioned above this is the limit of large Bond number. The density difference $\Delta\rho$ between the two fluids is large compared to the density of the lighter fluid, and the denser fluid flows along the bottom of the cell which is a horizontal, impermeable surface. In doing so, the denser fluid displaces the lighter fluid out of its way. Here, the geometry is considered to be vertically unconfined so that the flow of the upper, lighter fluid is negligible.

Of interest is the evolution of the interface $h(x, t)$ between the two fluids. Owing to the vertically unconfined, long and thin geometry of the flow passage, the denser

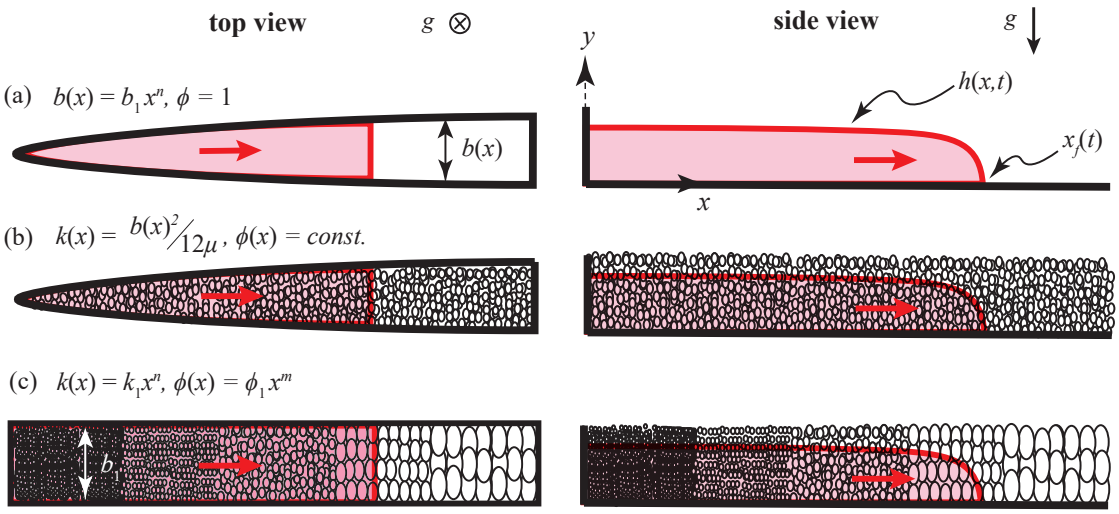

Fig. 2.1. A summary of the gravity current flows and domains considered in this work. (a) Flow away from the origin in a completely porous ($\phi = 1$) HS cell of variable width given by $b(x) = b_1 x^n$ ($b_1 = const.$, $0 \leq n < 1$). (b) Flow in uniformly porous ($\phi = \phi_1 = const. \neq 1$) passage of variable width given by the same $b(x)$ as in (a). (c) Flow in a uniform-width slab (i.e., $b(x) = b_1 = const.$) with horizontally heterogeneous porosity and permeability given by $\phi(x) = \phi_1 x^m$ and $k(x) = k_1 x^n$ respectively. The effective permeability of the medium in (a) and (b) is set by the Hele-Shaw analogy via the width: $k(x) = [b(x)]^2/(12\mu)$. Figure reproduced and adapted with permission from [Zheng et al., Influence of heterogeneity on second-kind self-similar solutions for viscous gravity currents, J. Fluid Mech., vol. 747, p. 221] © Cambridge University Press 2014.

fluid has a slender profile (low aspect ratio) and its flow is described by *lubrication theory*. The lubrication approximation also requires that viscous forces dominate inertia forces; this is the limit of small Reynolds number. Therefore, in the regime, the flow is governed by a balance of viscous forces and gravity. Furthermore, the lubrication approximation allows for (at the leading order in the aspect ratio) the variation of quantities across the transverse direction, as well as the vertical velocities of the fluids to be neglected during the mathematical analysis of the flow.

As shown in Figure 2.1(a), for the flow in a HS cell, the cell's width varies as a power-law of the streamwise coordinate x, i.e., $b(x) = b_1 x^n$, where $n \geq 0$ is a dimensionless exponent, and $b_1 > 0$ is a dimensional consistency constant having units m^{1-n}. Non-unit porosity can also be modelled by filling the HS cell with beads of fixed diameter as illustrated in Figure 2.1(b). Since the cell has a variable width, it originates from a cell 'origin,' which is always taken to be $x = 0$ such that $b(0) = 0$. As discussed in [38], in such a flow geometry, the lubrication approximation may fail when $b(x)$ is an increasing function of x i.e., $\mathrm{d}b/\mathrm{d}x = nb_1 x^{n-1} > 1$. In such quickly-widening cells, the transverse variations of properties become significant. The validity of the lubrication approximation, and models derived on the basis of it, is here ensured by only considering $n < 1$ such that $b(x)$ remains a decreasing function of x.

As shown in Figure 2.1(c), the present model could be expanded to also consider a gravity current spreading horizontally in a porous slab of constant transverse width ($b(x) = b_1 = const.$) with heterogeneous porosity $\phi(x) = \phi_1 x^m$ and permeability $k(x) = k_1 x^n$, which vary in the streamwise coordinate (see, e.g., [38]). Here, $m, n \geq 0$ are dimensionless exponents and $\phi_1, k_1 > 0$ are dimensional constants needed for consistency with the definitions of porosity and permeability, respectively; specifically ϕ_1 has units of units of m^{-m}, and k_1 has units of m^{2-n}. These variations are illustrated by the streamwise changes of bead radii in Figure 2.1(c). Now, the point at which the porosity and permeability vanishes becomes the origin of the cell. Another interesting case, that of a medium with vertically heterogeneous porosity, has been explored by Ciriello et al. [50]. In this thesis, modelling efforts are limited to flows in a completely porous (i.e., unobstructed, $\phi = 1$) HS cells of variable width as in Figure 2.1(a). However, the numerical scheme developed herein can readily treat any of these cases, taking the appropriate parameter definitions from Table 2.2, as discussed in Section 2.2.

The denser fluid is allowed to be a non-Newtonian fluid. Specifically, it is assumed to obey the power-law rheology; this is also known as the Oswald–de Weale fluid [39]. In unidirectional flow, the shear stress is given by $\tau = \mu(\dot{\gamma})\dot{\gamma}$, where the dynamic

viscosity μ depends on the shear rate $\dot{\gamma}$ as $\mu(\dot{\gamma}) = \mu_0\dot{\gamma}^{r-1}$. Here, μ_0 is the flow consistency index (units of Pa·s^r), and r (> 0) is the fluid rheological index. Fluids having $r < 1$ are termed shear-thinning (e.g., blood), and fluids with $r > 1$ are termed shear-thickening (e.g., dense particulate suspensions). In the special case of $r = 1$, the power-law model reduces to the Newtonian fluid, and μ_0 is precisely the 'classical' shear viscosity. As stated above, the nature of the displaced fluid is immaterial to the dynamics of the viscous gravity current, as long as the viscosity and density contrast is large. This condition was satisfied, for example, by assuming (for the purposes of this chapter) that air is the displaced fluid.

Finally, the volume of the fluid in the cell itself may be either fixed (constant mass) or vary with time (injection). Consistent with the literature, the instantaneous volume of fluid in the cell is allowed to increase as a power law in t: $\mathcal{V}(t) = \mathcal{V}_0 + \mathcal{V}_{\text{in}} t^{\alpha}$, where $\mathcal{V}_0$ is the initial volume of fluid in the HS cell (measured in m^3), $\alpha \geq 0$ is a dimensionless exponent, and $\mathcal{V}_{in}$ is an injection pseudo-rate (in units m^{3}s$^{-\alpha}$), becoming precisely the injection rate for $\alpha = 1$. Section 2.2 discusses how this assumption lead to BCs for the physical problem and for the numerical scheme.

2.2 Governing Equation, Initial and Boundary Conditions

The propagation of a viscous gravity current is described by a diffusion equation for the interface $h(x,t)$ between the fluids, which is also the shape of profile of the denser fluid. The models are derived either from porous medium flow under Darcy's law and the Dupoit approximation [25, Ch. 8] or using lubrication theory with no-slip along the bottom of the cell and zero shear stress at the fluid–fluid interface [20, Ch. 6-C]. The resulting velocity field is combined with a depth-averaged form of the continuity equation to derive the nonlinear parabolic PDE for $h(x,t)$. To summarize all gravity current propagation along horizontal surfaces, a single 'thin-film' [56] equation is proposed:

$$\frac{\partial h}{\partial t} = \frac{A}{x^p}\frac{\partial}{\partial x}\left(x^q \psi \frac{\partial h}{\partial x}\right). \tag{2.1}$$

According to Engelbrecht [57, Ch. 5], Equation (2.1) can be classified as an 'evolution equation.' The term in the parentheses on the right-hand side of Equation (2.1), roughly, represents a fluid flux balanced by the change in height on the left-hand side. The multiplicative factor A/x^p arises due to (i) geometric variations of the flow passage in the flow-wise direction, (ii) porosity variations in the flow-wise direction, or (iii) from the choice of coordinate system in the absence of (i) or (ii). Here, A is a dimensional constant depending on the flow geometry and domain, and fluid characteristics. Additionally, p and q are dimensionless exponents that depend on the flow geometry and fluid rheology. The quantity denoted by ψ represents specifically the *nonlinearity* in these PDEs, thus it is necessarily a function of h, and possibly $\partial h/\partial x$ for a non-Newtonian fluid (as in the second, third and fourth rows of Table 2.2).[1]

As stated in Section 1, several versions of Equation (2.1) were explored herein, incorporating geometric variations, porosity variations, non-Newtonian behavior. Several classical cases of gravity currents in porous media are listed in Table 2.1, which lists expressions for A, p, q and ψ. However, the crux of this thesis is the numerical simulation of non-Newtonian gravity currents and some pertinent physical scenarios that were tackled using the numerical scheme developed herein are presented in Table 2.2.

In this study, the PDE (2.1) was solved on the finite space-time interval $(x, t) \in [\ell, L] \times [t_0, t_f]$. Here, t_0 and t_f represent the initial and final times of the numerical simulation's run, respectively. An initial condition (IC) $h_0(x)$ was specified at $t = t_0$, so that $h(x, t_0) = h_0(x)$ was known. Meanwhile, ℓ is a small positive value (close to 0). Boundary conditions (BCs) are specified at $x = \ell$ and $x = L$. These involve some combination of h and $\partial h/\partial x$. The reason for taking $x = \ell \neq 0$ will become clear when these BCs are derived below.

[1]Interestingly, an 'r-Laplacian' PDE similar to Equation (2.1) for a power-law fluid in a HS cell (second row of Table 2.2) arises during fluid–structure interaction between a power-law fluid and an enclosing slender elastic tube [58]. This PDE can also be tackled by the proposed finite-difference scheme.

Having established the PDE (2.1) it is now pertinent to devise a suitable set of BCs. The BCs are based on the imposed mass conservation/growth constraint. Consider the case of a viscous gravity current in a porous slab with variable porosity $\phi(x) = \phi_1 x^m$, and transverse width $b_1 = const$. Then, the conservation of mass constraint (see [38]) takes the form

$$\int_\ell^L h(x,t)\, b_1\, \phi(x)\, \mathrm{d}x = \mathcal{V}_0 + \mathcal{V}_{\text{in}} t^\alpha, \tag{2.2}$$

where $\alpha \geq 0$. In the parallel case of a HS cell with variable width, $b(x) = b_1 x^n$, and porosity $\phi_1 = const.$, which can either be set to 1 or absorbed into b_1, the mass constraint becomes

$$\int_\ell^L h(x,t)\, b(x)\, \mathrm{d}x = \mathcal{V}_0 + \mathcal{V}_{\text{in}} t^\alpha. \tag{2.3}$$

Taking a time derivative of Equation (2.3) and employing Equation (2.1), the following is obtained

$$\begin{aligned}\frac{\partial}{\partial t}\int_\ell^L h(x,t) b_1 x^n\, \mathrm{d}x = \int_\ell^L \frac{\partial h}{\partial t} b_1 x^n\, \mathrm{d}x = \int_\ell^L b_1 x^n \frac{A}{x^n}\frac{\partial}{\partial x}\left(x^q \psi \frac{\partial h}{\partial x}\right) \mathrm{d}x \\ = A b_1 \left(x^q \psi \frac{\partial h}{\partial x}\right)\Bigg|_{x=\ell}^{x=L} \overset{\text{by (2.3)}}{=} \frac{\mathrm{d}(\mathcal{V}_{\text{in}} t^\alpha)}{\mathrm{d}t} = \alpha \mathcal{V}_{\text{in}} t^{\alpha-1}.\end{aligned} \tag{2.4}$$

Here, $p = n$ in this case of interest, as described in Table 2.2, and $Ab_1 = const$. Thus, conditions relating $x^q \psi \partial h/\partial x$ at $x = \ell$ and $x = L$ to $\alpha \mathcal{V}_{\text{in}} t^{\alpha-1}$ are obtained. These conditions, if satisfied, automatically take into account the imposed volume constraint from Equation (2.3). The calculation starting with Equation (2.2) is omitted here as it is identical, subject to proper choice of p.

For the case of propagation away from the cell's origin (i.e., any injection of mass must occur near $x = 0$, specifically at $x = \ell$), to satisfy Equation (2.4), it follows that

$$\left(x^q \psi \frac{\partial h}{\partial x}\right)\Bigg|_{x=\ell} = \begin{cases} -\frac{\alpha B}{A} t^{\alpha-1}, & \alpha \neq 0, \\ 0, & \alpha = 0, \end{cases} \tag{2.5a}$$

$$\left(\psi \frac{\partial h}{\partial x}\right)\Bigg|_{x=L} = 0 \quad \Leftarrow \quad \frac{\partial h}{\partial x}\Bigg|_{x=L} = 0, \tag{2.5b}$$

where $B = \mathcal{V}_{\text{in}}/b_1$. The case of $\alpha > 0$ represents mass injection into the system. Although Equation (2.3) and Equations (2.5) are equivalent, the imposition of the nonlinear BC in Equations (2.5a) must be approached with care. It should be clear that to impose a flux near the origin (at $x = 0$), $\left(x^q \psi \partial h/\partial x\right)\big|_{x\to 0}$ must be finite. Then, $\psi \partial h/\partial x = \mathcal{O}(1/x^q)$ as $x \to 0$. On the spatial domain $x \in (0, L)$, such an asymptotic behavior is possible for $p = q = 0$. However, for cases in a variable width cell ($p, q \neq 0$), the local profile and slope as $x \to 0$ blow up if they are to satisfy $\psi \partial h/\partial x = \mathcal{O}(1/x^q)$ as $x \to 0$. To avoid this uncomputable singularity issue, the computational domain was defined to be $x \in (\ell, L)$, where ℓ is 'small' but > 0. The BC from Equation (2.5a) at $x = \ell$ can then be re-written as

$$\left(\psi \frac{\partial h}{\partial x}\right)\bigg|_{x=\ell} = -\frac{\alpha B}{A\ell^q} t^{\alpha-1}, \qquad \alpha > 0. \tag{2.6}$$

In the study of second-kind similarity in these flows it is also of interest to consider the case of a gravity current released a finite distance away from the origin and then spreading towards the origin. In this case, an additional length scale arises in the problem: the initial distance of the current's edge from the origin, say $x_f(0)$. The existence of this extra length scale complicates the self-similarity analysis [23, Ch. 4], as discussed in Section 1. However, the proposed numerical scheme can handle this case without significant problem; in fact, it requires no special consideration, unlike spreading away from the origin. Now, is permitted to simply take $\ell = 0$ and consider spreading on the domain $(0, L)$ subject to the following BCs:

$$\left(x^q \psi \frac{\partial h}{\partial x}\right)\bigg|_{x\to 0} = 0 \quad \Leftarrow \quad \frac{\partial h}{\partial x}\bigg|_{x=0} = 0, \tag{2.7a}$$

$$\left(\psi \frac{\partial h}{\partial x}\right)\bigg|_{x=L} = \begin{cases} \frac{\alpha B}{AL^q} t^{\alpha-1}, & \alpha \neq 0, \\ 0, & \alpha = 0, \end{cases} \tag{2.7b}$$

which together satisfy Equation (2.4) and, thus, Equation (2.3).

The most significant advantage of defining nonlinear flux BCs, such as those in Equations (2.5) or (2.7), is that a nonlinear nonlocal (integral) constraint, such as that in Equation (2.2) or (2.3), no longer has to be applied onto the solution $h(x, t)$.

Furthermore, upon beginning the analysis with compact initial conditions, i.e., there exists a nose location $x = x_f(t_0)$ such that $h\big(x_f(t_0), t_0\big) = 0$, following which the finite-speed of propagation property of the nonlinear PDE (2.1) [17, 18] ensured that this nose $x_f(t)$ existed for all $t > t_0$ and $h\big(x_f(t), t\big) = 0$ as well. The proposed fully-implicit scheme naturally captures this feature of the PDE, without any numerical instability, and is therefore always implemented the *fixed* domain $x \in (\ell, L)$ instead of attempting to rescale to a moving domain on which $x_f(t)$ is one of the endpoints. The latter approach proposed by Bonnecazze et al. [59] (and used in more recent works [60] as well) led to a number of additional variable-coefficient terms arising in the PDE (2.1), due to the non-Galilean transformation onto a shrinking/expanding domain. From a numerical methods point of view, having to discretize these additional terms is not generally desirable.

Having defined a suitable set of BCs, the last remaining piece of information required to close the statement of the mathematical problem at hand is the selection of a pertinent IC. For the case of the release of a finite fluid mass ($\alpha = 0$), an arbitrary polynomial initial condition may be selected, as long as it has zero slope at the origin ($x = 0$), leading to satisfaction of the no-flux boundary condition (2.5a). To this end, the IC was selected to be represented by

$$h_0(x) = \begin{cases} \frac{3}{2} C_0 \left(x_0^\gamma - x^\gamma \right), & x \leq x_0, \\ 0, & x > x_0, \end{cases} \tag{2.8}$$

where x_0 is a 'release-gate' location defining the initial position of the current's nose, i.e., $x_0 = x_f(t_0)$ and $h\big(x_f(t_0), t_0\big) \equiv h_0(x_0) = 0$. The constant $\gamma > 1$ is an arbitrary exponent. Finally, C_0 was set by normalizing $h_0(x)$ such that the initial volume of fluid corresponds to the selected fluid volume, $\mathcal{V}_{\text{in}}$, via Equation (2.3).

The case of the release of a finite mass of fluid is particularly forgiving in how the IC is set, particularly with respect to its slope at $x = 0$. In fact, it is observed that setting $\gamma = 1$ in Equation (2.8) resulted in the scheme providing an initial flux of fluid at $t = t_0^+$, with $(\partial h/\partial x)_{x=0}$ thereafter. On the other hand, the case

of mass injection ($\alpha \neq 0$) governed by the nonlinear BC is not as forgiving. By virtue of the 'point-source' mass injection at $x = \ell$, the slope at the origin sharply rises from the moment of mass injection. This very sharp rise has a tendency to introduce unphysical oscillations in the current profile when starting from the IC in Equation (2.8). To avoid this, a 'better' IC was selected, which has a shape more similar to the diverging solution near $x = 0$. Having tested a few different options, it is found that an exponential function worked well:

$$h_0(x) = \begin{cases} -a + be^{cx}, & x \leq x_0, \\ 0, & x > x_0. \end{cases} \tag{2.9}$$

Here, a, b and c are positive constants, and $x_0 = \frac{1}{c} \ln \frac{a}{b}$ ensures that the IC has no negative values and a sharp front.

Finally, it should be noted that the IC from Equation (2.8) was not used in the convergence studies for finite initial mass (Section 4.1.1 and Section 4.1.2). Rather, the IC was taken to be the exact self-similar solution of Ciriello et al. [50] for a power-law non-Newtonian fluid in a uniform-width ($n = 0$) HS cell (see also Appendix A). The reasoning behind this particular choice of IC is further expounded upon in Section 4.1.

Table 2.1.
Selected classical models of the propagation of Newtonian ($\mu = \mu_0$) viscous gravity currents, which can be simulated by the proposed finite-difference scheme. Unless otherwise stated the porosity $\phi = 1$.

Case	A	p	q	ψ
Fixed-width HS cell: $b(x) = b_1$, (see Huppert [29])	$\dfrac{\Delta\rho g b_1^2}{12\mu_0}$	0	0	h
2D unconfined domain ($s = 0$) or 3D axisymmetric domain ($s = 1$). (see Huppert [19])	$\dfrac{\Delta\rho g}{3\mu_0}$	s	s	h^3
2D axi-symmetric domain ($s = 1$) or 3D spherically-symmetric domain ($s = 2$), const. porosity: $\phi(x) = \phi_1$, const. permeability $k(x) = k_1$. (see Barrenblatt [3]†)	$\dfrac{\Delta\rho g k_1}{\mu_0\phi_1}$	s	s	h
2D porous medium, var. porosity: $\phi(x) = \phi_1 x^m$, var. permeability: $k(x) = k_1 x^n$. (see Zheng et al. [38])	$\dfrac{\Delta\rho g k_1}{\mu_0\phi_1}$	m	n	h

† For more recent analyses of this case, also see Huppert and Woods [29], Lyle et al. [31].

Table 2.2.
Further models of the propagation of viscous gravity currents, including non-Newtonian ones, which can be simulated by the proposed finite-difference scheme.

Case	A	p	q	ψ
Newtonian fluid: $\mu = \mu_0$, var. width HS cell: $b(x) = b_1 x^n$. (see Zheng et al. [38])	$\dfrac{\Delta\rho g b_1^2}{12\mu_0}$	n	$3n$	h
Power-law fluid: $\mu = \mu_0 \dot{\gamma}^{r-1}$, var. width HS cell: $b(x) = b_1 x^n$. (see Di Federico et al. [49], Longo [61])	$\left(\dfrac{r}{2r+1}\right)\left(\dfrac{\Delta\rho g}{\mu_0}\right)^{1/r}\left(\dfrac{b_1}{2}\right)^{(r+1)/r}$	n	$n\left(\dfrac{2r+1}{r}\right)$	$h\left\lvert\dfrac{\partial h}{\partial x}\right\rvert^{(1-r)/r}$
Power-law fluid: $\mu = \mu_0 \dot{\gamma}^{r-1}$, 2D porous medium, var. porosity: $\phi(x) = \phi_1 x^m$, var. permeability: $k(x) = k_1 x^n$. (see Ciriello et al. [50])	$2^{(3r+1)/2}\left(\frac{r}{3r+1}\right)^{1/r}$ $\times\left(\frac{k_1}{\phi_1}\right)^{(r+1)/2r}\left(\frac{\Delta\rho g}{\mu_0}\right)^{1/r}$	m	$\frac{m(r-1)+n(r+1)}{2r}$	$h\left\lvert\dfrac{\partial h}{\partial x}\right\rvert^{(1-r)/r}$
Hershel-Buckley fluid: $\tau = \tau_y + \mu_0 \dot{\gamma}^r$, variable width HS cell: $b(x) = b_1 x^n$.† (see Di Federico et al. [49] and Longo [61])	$\left(\dfrac{r}{2r+1}\right)\left(\dfrac{\Delta\rho g}{\mu_0}\right)^{1/r}\left(\dfrac{b_1}{2}\right)^{(r+1)/r}$	n	$n\left(\dfrac{2r+1}{r}\right)$	$h\left\lvert\frac{\partial h}{\partial x}\right\rvert^{(1-r)/r}(1-\mathcal{K})^{(r+1)/r}$ $\times\left[1+\left(\frac{r}{r+1}\right)\mathcal{K}\right]$

† $\tau(\dot{\gamma})$ is the viscous shear stress and τ_y is the fluid yield stress (both in Pa), $\mathcal{K} = (\mathfrak{K}/x^k)\,|\partial h/\partial x|^{-1}$, where $\mathfrak{K} = (2\tau_y)/(\Delta\rho g b_1)$.

3. THE NUMERICAL SCHEME

The proposed numerical method is a one-dimensional finite-difference scheme using the Crank–Nicolson approach toward implicit time-stepping. This presentation follows recent literature, specifically the construction in [38, Appendix B]. The proposed scheme's truncation error is formally of second order in both space and time, and the scheme is expected to be unconditionally stable. Furthermore, the scheme is conservative in the sense that it maintains the imposed time-dependency of the fluid volume with high accuracy via a specific set of nonlinear BCs. This chapter is devoted to discussing all these topics one by one.

3.1 Notation: Grids, Time Steps, and Grid Functions

The PDE (2.1) is solved on an equispaced one-dimensional grid of $N+1$ nodes with grid spacing $\Delta x = (L-\ell)/(N-1)$. The solution values are kept on a staggered grid of cell-centers, which are offset by $\Delta x/2$ with respect to the equispaced grid points. As a result, there is a node lying a half-grid-spacing beyond each domain boundary. It follows that the location of the ith grid point on the staggered grid is $x_i = \ell + (i-1/2)\Delta x$, where $i = 0, 1, 2, \ldots, N$. A representative grid with 12 nodes is shown in Figure 3.1. The use of a staggered grid affords additional stability to the scheme and allows the numerical discretization of Neumann BCs to be second-order accurate by default, using only two cell-centered values (as the boundary now lies half-way between two grid points).

As stated in Section 2.2, the PDE (2.1) is solved over a time period $t \in (t_0, t_f]$, such that $t_f > t_0 \geq 0$, where both the initial time t_0 and the final time t_f of the simulation are user defined. The scheme thus performs M discrete time steps each of size $\Delta t = (t_f - t_0)/(M-1)$. The nth time step advances the solution to $t = t^n \equiv$

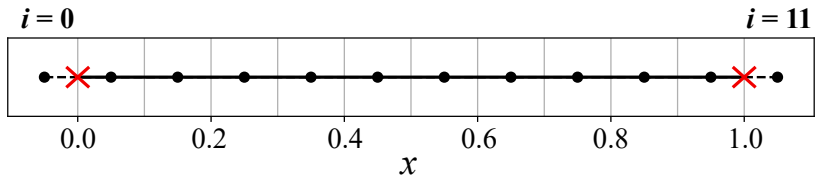

Fig. 3.1. A sample twelve-node equispaced, staggered, one-dimensional grid. The grid nodes are staggered by half a grid step $\Delta x/2$ from the cell faces. The actual domain boundaries are marked by x. Here, $\ell = 0$ and $L = 1$.

$t_0 + n\Delta t$, where $n = 0, 1, \ldots, M-1$. Finally, it is pertinent to define the discrete analog ('grid function') to the continuous gravity current shape, which is actually solved for, by $h_i^n \approx h(x_i, t^n)$.

3.2 The Nonlinear Crank–Nicolson Scheme

The operator $\mathcal{L}$ denotes the continuous spatial operator acting on h on the right-hand side of Equation (2.1), i.e.,

$$\mathcal{L}[h] \equiv \frac{A}{x^p}\frac{\partial}{\partial x}\left(x^q \psi \frac{\partial h}{\partial x}\right). \tag{3.1}$$

Since $\mathcal{L}$ is a second-order spatial operator and, thus, Equation (2.1) is a diffusion equation, there is an inclination to implement second-order-accurate time-stepping by the Crank–Nicolson scheme [62]. The Crank–Nicolson approach makes the scheme fully implicit, hence avoiding the stringent restriction ($\Delta t \lesssim (\Delta x)^2$) suffered by explicit time discretizations of diffusion equations [63, Ch. 6]. Then, the time-discrete version of Equation (2.1) becomes

$$\frac{h_i^{n+1} - h_i^n}{\Delta t} = \frac{1}{2}\big(\mathcal{L}_d\left[h_i^{n+1}\right] + \mathcal{L}_d\left[h_i^n\right]\big), \tag{3.2}$$

where $\mathcal{L}_d$ is the discrete analog to the continuous spatial operator $\mathcal{L}$ defined in Equation (3.1). Based on the approach of Christov and Homsy [64], the discrete spatial

operator is constructed via flux-conservative central differencing using two cell-face values, while staggering the nonlinear terms:

$$\mathcal{L}_d\left[h_i^n\right] = \frac{A}{x_i^p}\left[\frac{\left(x_{i+1/2}^q \psi_{i+1/2}^{n+1/2}\right) S_{i+1/2}^n - \left(x_{i-1/2}^q \psi_{i-1/2}^{n+1/2}\right) S_{i-1/2}^n}{\Delta x}\right], \tag{3.3a}$$

$$\mathcal{L}_d\left[h_i^{n+1}\right] = \frac{A}{x_i^p}\left[\frac{\left(x_{i+1/2}^q \psi_{i+1/2}^{n+1/2}\right) S_{i+1/2}^{n+1} - \left(x_{i-1/2}^q \psi_{i-1/2}^{n+1/2}\right) S_{i-1/2}^{n+1}}{\Delta x}\right], \tag{3.3b}$$

where $S \equiv \partial h/\partial x$ is the slope of the gravity current's shape. Note that the nonlinear terms, denoted by ψ, are evaluated the same way, i.e., at the mid-time-step $n+1/2$, for both $\mathcal{L}_d\left[h_i^n\right]$ and $\mathcal{L}_d\left[h_i^{n+1}\right]$.

Substituting Equations (3.3) into Equation (3.2) results in a system of *nonlinear* algebraic equations because ψ is evaluated at mid-time-step $n+1/2$ and, thus, depends on both h_i^n (known) and h_i^{n+1} (unknown). This system has to be solved for the vector h_i^{n+1} $(i = 0, \ldots, N)$, i.e., the approximation to the gravity current's shape at the next time step. Solving a large set of nonlinear algebraic equations can be tedious and computationally expensive. A simple and robust approach to obtaining a solution of the nonlinear algebraic system is through fixed-point iterations, or 'the method of internal iterations' [65]. Specifically, it is hence possible to iteratively compute approximations to h_i^{n+1}, the grid function at the new time step, by replacing it in Equation (3.2) with $h_i^{n,k+1}$, where $h_i^{n,0} \equiv h_i^n$. Then, the proposed numerical scheme takes the form:

$$\begin{aligned}\frac{h_i^{n,k+1} - h_i^n}{\Delta t} =& \frac{A}{2\Delta x}\left[\frac{x_{i+1/2}^q}{x_i^p}\psi_{i+1/2}^{n+1/2,k} S_{i+1/2}^{n,k+1} - \frac{x_{i-1/2}^q}{x_i^p}\psi_{i-1/2}^{n+1/2,k} S_{i-1/2}^{n,k+1}\right] \\ &+ \frac{A}{2\Delta x}\left[\frac{x_{i+1/2}^q}{x_i^p}\psi_{i+1/2}^{n+1/2,k} S_{i+1/2}^{n} - \frac{x_{i-1/2}^q}{x_i^p}\psi_{i-1/2}^{n+1/2,k} S_{i-1/2}^{n}\right].\end{aligned} \tag{3.4}$$

The key idea in adopting the method of internal iterations is to evaluate the nonlinear ψ terms from information known at iteration k and the previous time step n, while keeping the linear slopes S from the next time step $n+1$ at iteration $k+1$. This manipulation linearizes the algebraic system, at the cost of requiring iterations over k. Upon convergence of the internal iterations, h_i^{n+1} is simply the last iterate $h_i^{n,k+1}$.

Prior to further discussing the iterations themselves or their convergence, it is now necessary to establish discrete approximations for ψ and S.

The operator $\mathcal{L}_d$ is essentially a second derivative, and hence should be treated along the lines of the standard way of constructing the three-point central finite-difference formula for the second derivative [63]. Therefore, $S_{i\pm1/2}$ can be discretized using a two-point central-difference approximation on the staggered grid. For example, at any time step:

$$S_{i+1/2} \equiv \left(\frac{\partial h}{\partial x}\right)_{x=x_{i+1/2}} \approx \frac{h_{i+1} - h_i}{\Delta x}. \tag{3.5}$$

Next, following [38, 66], ψ at $x_{i\pm1/2}$ is evaluated by averaging the known values at x_i and x_{i+1} or x_i and x_{i-1}, respectively. Likewise, to approximate $\psi^{n+1/2}$, an average of the known values: ψ^n at t^n and $\psi^{n,k}$ at the previous internal iteration is evaluated. In other words, approximation of the nonlinear terms becomes

$$\psi_{i+1/2}^{n+1/2,k} = \frac{1}{2}\left[\underbrace{\frac{1}{2}\left(\psi_{i+1}^{n,k} + \psi_i^{n,k}\right)}_{=\psi_{i+1/2}^{n,k}} + \underbrace{\frac{1}{2}\left(\psi_{i+1}^{n} + \psi_i^{n}\right)}_{=\psi_{i+1/2}^{n}}\right], \tag{3.6a}$$

$$\psi_{i-1/2}^{n+1/2,k} = \frac{1}{2}\left[\underbrace{\frac{1}{2}\left(\psi_{i}^{n,k} + \psi_{i-1}^{n,k}\right)}_{=\psi_{i-1/2}^{n,k}} + \underbrace{\frac{1}{2}\left(\psi_{i}^{n} + \psi_{i-1}^{n}\right)}_{=\psi_{i-1/2}^{n}}\right]. \tag{3.6b}$$

Equations (3.6) afford improved stability for nonlinear PDEs, while preserving the conservative nature of the scheme (as will be shown in Section 4.2), as discussed by Von Rosenberg [67] who credited the idea of averaging nonlinear terms across time stages and staggered grid points to the seminal work of Douglas Jr. [68, 69]. The scheme thus described is depicted by the stencil diagram in Figure 3.2.

Here, it is worthwhile noting that, while the classical Crank–Nicolson [62] scheme is *provably* unconditionally stable [63] when applied to a *linear* diffusion equation, it was suggested in [64] that the current approach provides additional stability to this nonlinear scheme even at large time steps. Since the current problem is nonlinear, some care has be taken in evaluating how large of a time step could be taken.

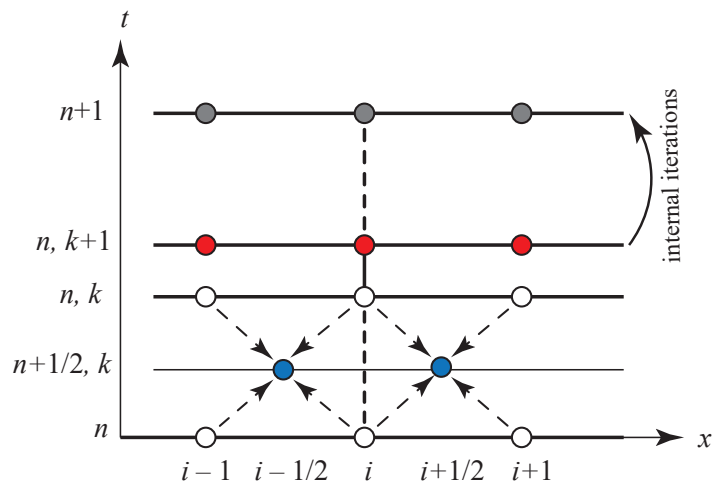

Fig. 3.2. Representative stencil of the proposed scheme's implementation on a staggered grid with internal iterations. After performing k internal iterations, the nonlinear terms $\psi_{i\pm1/2}$ are evaluated at stage "$n+1/2, k$" (highlighted blue) from the known quantities h_i^n and $h_i^{n,k}$. The unknown quantity $h_i^{n,k+1}$ at the next internal iteration, $n, k+1$, is found by solving the linear system in Equation (3.9). The process continues until the convergence criterion from Equation (3.10) is met.

Nevertheless, it was still expected that the largest stable Δt will be independent of Δx.

In the context of this problem, the case of interest of a power-law non-Newtonian viscous gravity current spreading in a variable width cell provides additional complications. Recalling Table 2.2, this model features $\partial h/\partial x$ in ψ, *unlike* the Newtonian case. While the temporal accuracy of the scheme is ensured through the robust implementation of the nonlinear Crank–Nicolson time-stepping, the spatial accuracy is contingent upon the discretization of $\partial h/\partial x$ in ψ. A further consequence is that, once $\partial h/\partial x$ is discretized, the discretization of ψ becomes *nonlocal* (i.e., it requires information beyond the ith grid point). Nevertheless, the overall scheme only requires

a three-point stencil for $\mathcal{L}_d$. In particular, for interior grid points, it is possible to use a central-difference formula, giving rise to the expression (at any time step):

$$\psi_i \equiv \left[h \left| \frac{\partial h}{\partial x} \right|^{(1-r)/r} \right]_{x=x_i} \approx h_i \left| \frac{h_{i+1} - h_{i-1}}{2\Delta x} \right|^{(1-r)/r}. \tag{3.7}$$

This choice of approximation ensures second-order accuracy at all interior grid nodes. However, at the second ($i = 1$) and the penultimate ($i = N - 1$) nodes, the second-order accurate approximation to $\partial h/\partial x$ in $\psi_{i\pm 1/2}$ as defined in Equations (3.6) requires the unknown values h_{-1} and h_{N+1}, which lie outside the computational domain. To resolve this difficulty, 'biased' (backward or forward) three-point difference approximations are used:

$$\psi_0 \approx h_0 \left| \frac{-3h_0 + 4h_1 - h_2}{2\Delta x} \right|^{(1-r)/r}, \tag{3.8a}$$

$$\psi_N \approx h_N \left| \frac{3h_N - 4h_{N-1} + h_{N-2}}{2\Delta x} \right|^{(1-r)/r}. \tag{3.8b}$$

Finally, substituting the discretization for S from Equation (3.5) into Equation (3.4), it is possible to re-arrange the scheme into a tridiagonal matrix equation:

$$\begin{aligned}
&\underbrace{\left[-\frac{A\Delta t}{2(\Delta x)^2} \frac{x^q_{i-1/2}}{x^p_i} \psi^{n+1/2,k}_{i-1/2} \right]}_{\text{matrix subdiagonal coefficient}} h^{n,k+1}_{i-1} \\
&\quad + \underbrace{\left[1 + \frac{A\Delta t}{2(\Delta x)^2} \left(\frac{x^q_{i+1/2}}{x^p_i} \psi^{n+1/2,k}_{i+1/2} + \frac{x^q_{i-1/2}}{x^p_i} \psi^{n+1/2,k}_{i-1/2} \right) \right]}_{\text{matrix diagonal coefficient}} h^{n,k+1}_{i} \\
&\quad + \underbrace{\left[-\frac{A\Delta t}{2(\Delta x)^2} \frac{x^q_{i+1/2}}{x^p_i} \psi^{n+1/2,k}_{i+1/2} \right]}_{\text{matrix superdiagonal coefficient}} h^{n,k+1}_{i+1} \\
&= h^n_i + \frac{A\Delta t}{2(\Delta x)^2} \left[\frac{x^q_{i+1/2}}{x^p_i} \psi^{n+1/2,k}_{i+1/2} (h^n_{i+1} - h^n_i) - \frac{x^q_{i-1/2}}{x^p_i} \psi^{n+1/2,k}_{i-1/2} (h^n_i - h^n_{i-1}) \right]
\end{aligned} \tag{3.9}$$

for the interior grid points $i = 1, \ldots, N - 1$. In Equation (3.9) the right-hand side and the variable coefficients in brackets on the left-hand side are both known, based

on $h_i^{n,k}$, at any given internal iteration k. Then, each internal iteration involved the inversion of a tridiagonal matrix to solve for the grid function $h_i^{n,k+1}$. The inversion of this tridiagonal matrix can be performed efficiently with, e.g., 'backslash' in MATLAB. Subsequently, the coefficient matrix has to be recalculated for each internal iteration because of the dependency of $\psi_{i\pm1/2}^{n+1/2,k}$ on $h_i^{n,k}$ arising from Equations (3.6) and (3.7).

The iterations in Equation (3.9) are initialized with $h_i^{n,0} = h_i^n$ $(i = 0, \ldots, N)$ and continued until an iteration $k+1 = K$ is reached at which a 10^{-8} relative error tolerance is met. Specifically,

$$\max_{0\le i\le N} \left| h_i^{n,K} - h_i^{n,K-1} \right| < 10^{-8} \max_{0\le i\le N} \left| h_i^{n,K-1} \right| . \tag{3.10}$$

Typically only a small number (typically, less than a dozen) of internal iterations are required at each time step, making the scheme, overall, quite efficient.

The algebraic system defined in Equation (3.9) applies to all *interior* nodes, i.e., $i = 1, \ldots, N-1$. To complete the system, the rows $i = 0$ and $i = N$ have to be defined, which arise from the proper numerical approximation of the nonlinear BCs, which comes in Section 3.3. Upon completing the latter task successfully, $h_i^{n,K}$ becomes the grid function at the next time step h_i^{n+1} upon the completion of the internal iterations, following which the time stepping proceeds.

3.2.1 The Special Case of Linear Diffusion

A special case of the proposed finite-difference scheme can be considered by setting the dimensionless exponents $p = q = 0$ (i.e., no spatial variation of the diffusivity) and $\psi = 1$ (linear diffusion). Accordingly, Equation (3.9) can be simplified and rearranged in the form $(i = 1, \ldots, N-1)$:

$$\left[1 + \frac{A\Delta t}{(\Delta x)^2}\right] h_i^{n+1} = \frac{A\Delta t}{(\Delta x)^2} \left(h_{i-1}^{n+1} + h_{i+1}^{n+1} + h_{i-1}^n + h_{i+1}^n\right) + \left[1 + \frac{A\Delta t}{(\Delta x)^2}\right] h_i^n . \tag{3.11}$$

If the grid function $h_i^n \approx h(x_i, t^n)$ represents the temperature field along a one-dimensional rigid conductor situated on $x \in [\ell, L]$, Equation (3.11) is then the original

second-order (in space and time) numerical scheme proposed by Crank and Nicolson [62] to solve a linear (thermal) diffusion equation [63, Section 6.3]. As such, this simplification helps illustrate the mathematical roots of the current scheme, and how the classical work has been generalized.

3.3 Implementation of the Nonlinear Boundary Conditions

As discussed in section 2.2, the boundary conditions are a manifestation of the global mass conservation constraint, Equation (2.2) or (2.3), imposed on Equation (2.1). The BCs described in Equations (2.5) and (2.7) are defined at the 'real' boundaries of the domain, i.e., at $x = \ell$ and $x = L$. The numerical scheme implements these on the staggered grid. This allows for derivatives at $x = \ell$ and $x = L$ to be conveniently approximated using central difference formulas using two nearby staggered grid points. In this manner, the BC discretization maintains the scheme's second order accuracy in space and time. Accordingly, for the case of a current spreading away from the cell's origin, Equations (2.5) are discretized in a 'fully-implicit' sense (to further endow numerical stability and accuracy to the scheme [66]) as follows:

$$\psi_{1/2}^{n+1/2,k} \frac{1}{\Delta x}\left(h_1^{n,k+1} - h_0^{n,k+1}\right) = \begin{cases} -\frac{\alpha B}{A\ell^q} t^{\alpha-1}, & \alpha \neq 0, \\ 0, & \alpha = 0, \end{cases} \tag{3.12}$$

$$\frac{1}{\Delta x}\left(h_N^{n,k+1} - h_{N-1}^{n,k+1}\right) = 0. \tag{3.13}$$

Within the internal iterations, however, $\psi_{1/2}^{n+1/2,k}$ is known independently of $h_1^{n,k+1}$ and $h_0^{n,k+1}$. Hence, the first ($i = 0$) and last ($i = N$) rows in the tridiagonal matrix, whose interior rows are constructed from Equation (3.9), can now be expressed as

$$h_1^{n,k+1} - h_0^{n,k+1} = \begin{cases} -\dfrac{4\alpha B t^{\alpha-1}\Delta x}{A\ell^q(\psi_0^n + \psi_1^n + \psi_0^{n,k} + \psi_1^{n,k})}, & \alpha \neq 0, \\ 0, & \alpha = 0, \end{cases} \tag{3.14a}$$

$$h_N^{n,k+1} - h_{N-1}^{n,k+1} = 0. \tag{3.14b}$$

Similarly, the discretized BCs for spreading of a current towards the origin when released a finite distance away from the origin, can be derived from Equations (2.7). Then, the first ($i = 0$) and last ($i = N$) rows in the tridiagonal matrix are expressed as

$$h_1^{n,k+1} - h_0^{n,k+1} = 0, \tag{3.15a}$$

$$h_N^{n,k+1} - h_{N-1}^{n,k+1} = \begin{cases} \dfrac{4\alpha B t^{\alpha-1}\Delta x}{AL^q(\psi_{N-1}^n + \psi_{N-2}^n + \psi_{N-1}^{n,k} + \psi_{N-2}^{n,k})}, & \alpha \neq 0, \\ 0, & \alpha = 0. \end{cases} \tag{3.15b}$$

4. CONVERGENCE AND CONSERVATION PROPERTIES OF THE SCHEME

At this point, the numerical scheme and boundary conditions defined in Equations (3.9) and (3.14) form a complete description of the numerical solution to the parabolic PDE from Equation (2.1), for a gravity current propagating away from the origin. It has been claimed that the finite-difference scheme is conservative (i.e., it accurately maintains the imposed time-dependency of the fluid volume described in Equation (2.3)) and has second-order convergence. These aspects of the scheme will be substantiated in Section 4.1 and Section 4.2, respectively. The computational domain's dimensions, which are set by L and b_1, and the properties of fluid being simulated are summarized in Table 4.1. For definiteness, the fluid properties were taken to be those of 95% glycerol-water mixture in air at 20°C (see [70, 71]).

Table 4.1.
A summary of the simulation parameters used in convergence and conservation studies. The fluid was assumed to be a 95% glycerol-water mixture at 20°C. The width exponent n and fluid rheology index r were varied on a case-by-case basis to simulate different physical scenarios.

Parameter	Value	Units
Channel length L	0.75	m
Width coefficient b_1	0.01732	m^{1-n}
Total released mass w	0.3155	kg
Density ρ	1250.8	$\mathrm{kg/m^3}$
Consistency index ($r \neq 1$) or dynamic viscosity ($r = 1$) μ_0	0.62119	$\mathrm{Pa{\cdot}s}^r$

4.1 Estimated Order of Convergence

First, the formal order of accuracy of the proposed scheme was justified through carefully chosen numerical examples. To do so, successively 'more complicated' cases from a numerical perspective were considered. First, the case of a centrally released fixed mass of fluid propagating in two directions was simulated (Section 4.1.1). Second, the unidirectional spreading of a fixed mass of fluid was simulated (Section 4.1.2). Third, and last, the unidirectional spreading of a variable fluid mass was considered (Section 4.1.3), i.e., injection of fluid at the boundary was taken into account.

In each of these three cases, there is a need for a reliable benchmark solution against which the numerical solutions on successively refined spatial grids could be compared. For the case of the release of a fixed mass of fluid, an exact self-similar solution is provided by Ciriello et al. [50]. Specifically the solution considers a fixed mass ($\alpha = 0$) of a power-law fluid in uniform HS cell ($n = 0$). The derivation of the self-similar solution is briefly discussed in the Appendix. This solution was used as the benchmark. As mentioned in Section 1, parabolic equations 'forget' their IC and the solution becomes self-similar after some time. However, for a general PDE, it is difficult (if not impossible) to estimate how long this process takes. Therefore, to ensure a proper benchmark against the exact self-similar solution, the simulation was started with the exact self-similar solution evaluated at some non-zero initial time ($t_0 > 0$). Using the latter as the initial condition, the current was allowed to propagate up to a final time t_f, with the expectation that the current would thus remain in the self-similar regime for all $t \in (t_0, t_f]$. Comparing the final numerical profile with the exact self-similar solution at $t = t_f$ then allowed for a proper benchmark.

To quantify the error between a numerical solution h_{num} and a benchmark h_{exact} solution at $t = t_f$, three standard function-space norms are used [12]:

$$\|h_{\text{num}}(x,t_f) - h_{\text{exact}}(x,t_f)\|_{L^\infty} = \max_{x\in[\ell,L]} \left|h_{\text{num}}(x,t_f) - h_{\text{exact}}(x,t_f)\right|, \tag{4.1a}$$

$$\|h_{\text{num}}(x,t_f) - h_{\text{exact}}(x,t_f)\|_{L^1} = \int_\ell^L \left|h_{\text{num}}(x,t_f) - h_{\text{exact}}(x,t_f)\right| \,\mathrm{d}x, \tag{4.1b}$$

$$\|h_{\text{num}}(x,t_f) - h_{\text{exact}}(x,t_f)\|_{L^2} = \sqrt{\int_\ell^L \left|h_{\text{num}}(x,t_f) - h_{\text{exact}}(x,t_f)\right|^2 \,\mathrm{d}x}. \tag{4.1c}$$

Using a second-order trapezoidal rule for the integrals, the integrals definitions in Equations (4.1) are discretized and expressed in terms of the grid functions to define the 'errors':

$$L^\infty_{\text{error}} \equiv \max_{0\le i\le N} \left|h_i^M - h_{\text{exact}}(x_i,t_f)\right|, \tag{4.2a}$$

$$\begin{aligned} L^1_{\text{error}} \equiv \Delta x \Bigg\{ \frac{1}{2}\Big[\left|h_0^M - h_{\text{exact}}(x_0,t_f)\right| + \left|h_N^M - h_{\text{exact}}(x_N,t_f)\right| \Big] \\ + \sum_{i=1}^{N-1} \left|h_i^M - h_{\text{exact}}(x_i,t_f)\right| \Bigg\}, \end{aligned} \tag{4.2b}$$

$$\begin{aligned} L^2_{\text{error}} \equiv \Bigg[\Delta x \Bigg\{ \frac{1}{2}\Big[\left|h_0^M - h_{\text{exact}}(x_0,t_f)\right|^2 + \left|h_N^M - h_{\text{exact}}(x_N,t_f)\right|^2 \Big] \\ + \sum_{i=1}^{N-1} \left|h_i^M - h_{\text{exact}}(x_i,t_f)\right|^2 \Bigg\} \Bigg]^{1/2}, \end{aligned} \tag{4.2c}$$

where M is the time step at which $t^M = t_f$.

Since the solution actually has a corner (derivative discontinuity) at the nose (wavefront) $x_f(t)$ such that $h\big(x_f(t),t\big) = 0$, the propagating gravity current is in fact only a *weak* solution to the PDE [12]. Therefore, the L^∞ norm is not expected to be a good one to measure the error, and it is not expected the solution would 'live' in this function space. Nevertheless, numerical results showed convergence in the L^∞ norm. The natural functional space for solutions of Equation (2.1) is the space of integrable functions, i.e., L^1. Indeed, excellent second-order convergence is observed in this norm. For completeness, the L^2 norm (commonly the function-space setting for parabolic equations [12, Ch. 7]) was considered as well. While convergence close

to second order was observed in this norm as well, it was clearly not the 'natural' one for these problems either.

For the estimated-order-of-convergence study, Δx was successively halved on a domain of fixed length, such that on the cth iteration of the refinement, the grid spacing was $\Delta x_c = \Delta x_0/2^{c-1}$, where Δx_0 was the initial grid spacing. Doing so ensured a set of common grid points (corresponding to the same physical locations) between successively refined grids. The order-of-convergence was estimated from the error in the three norms considered, based on the expectation that at the cth refinement, the error L_{error} is proportional to $(\Delta x_c)^{\mathfrak{p}}$, where $\mathfrak{p}$ represents the estimated order-of-convergence to be determined. Hence, for any of the three L_{error} functions defined in Equations (4.2) above, it can be shown that

$$\mathfrak{p} = \frac{1}{c-1} \log_2 \left[\frac{L_{\text{error}}(\Delta x_0)}{L_{\text{error}}(\Delta x_c)} \right], \tag{4.3}$$

where $L_{\text{error}}(\Delta x)$ is the norm of the error evaluated on the grid with spacing Δx. In all studies in this section, a preliminary grid with $N = 101$ nodes was selected, and would remain the coarsest grid for the refinement study. Given the (formally) unconditionally stable nature of the scheme, $\Delta t = 2\Delta x$ was selected for the refinement studies without loss of generality. From a computational standpoint, it is desirable that time step and grid spacing are of the same order of magnitude in the estimated-order-of-convergence study.

4.1.1 Central Release of a Fixed Fluid Mass (No Boundary Effects)

For this benchmark, a symmetric domain $x \in [-L, +L]$ was considered. A fixed mass of fluid (i.e., $\alpha = 0$ in the volume constraint in Equation (2.3)) was released with an initial shape that was symmetric about $x = 0$. The final simulation time t_f was such that the gravity current did not reach $x = \pm L$ for $t \leq t_f$. Since the fluid mass was constant and the BCs are imposed at $x = \pm L$ (where $h = 0$ initially and remained so for all $t \leq t_f$, by construction), their discretization simply reduces to the simplest cases, i.e., Equations (3.15a) and (3.14b). Thus, the BCs for this

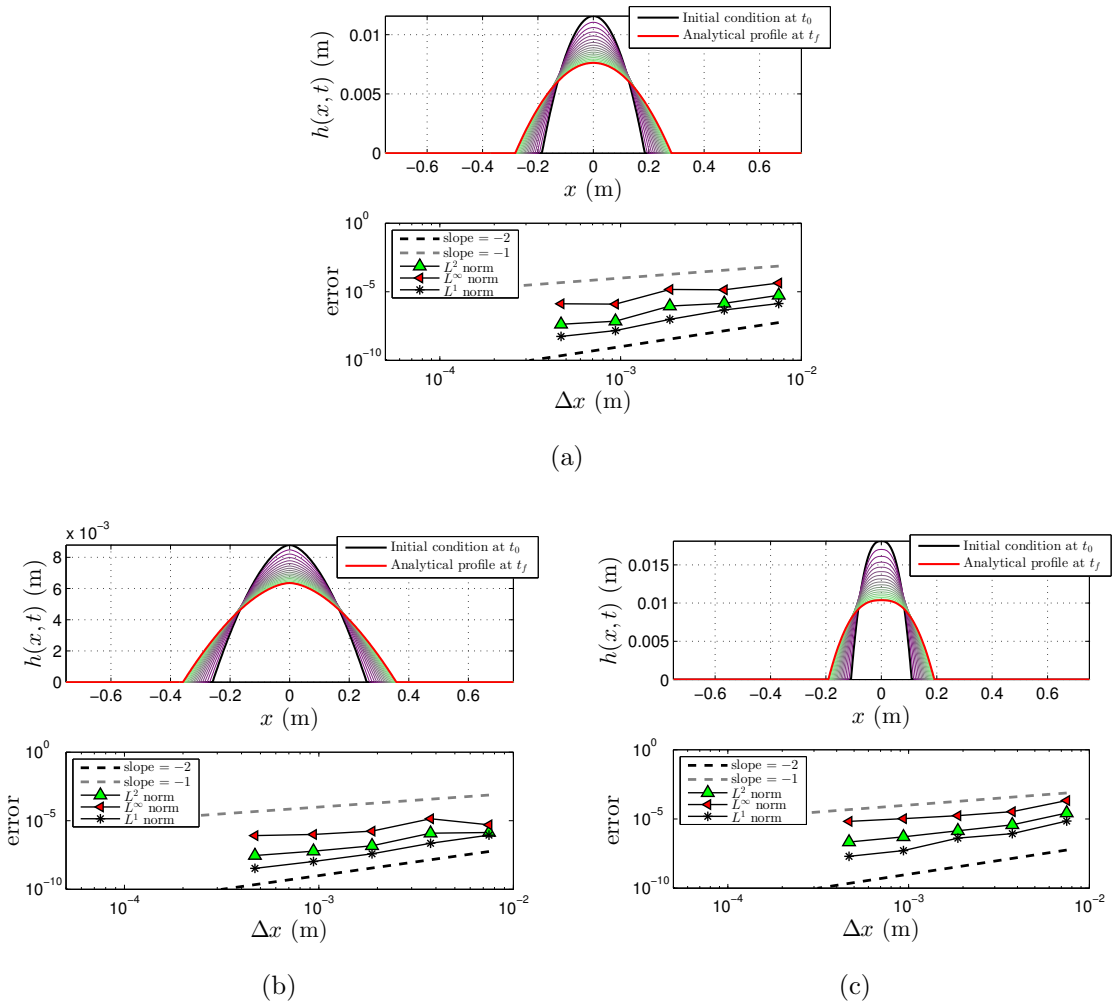

Fig. 4.1. Estimated order-of-convergence of a 'centrally released' fixed fluid mass propagating in both directions in a uniform-width HS cell ($n = 0$) for the case of (a) a Newtonian fluid ($r = 1$), (b) a Shear-thinning fluid ($r = 0.7$), and (c) a Shear-thickening fluid ($r = 1.6$). The currents' shapes are plotted from early times (purple/dark) to late times (green/light). In all cases, the volume of fluid is fixed $\mathcal{V} = 2.4902 \times 10^{-5}$ m^3 and $b_1 = 0.01739$ m. The currents were released at $t_0 = 1$ s and spread until $t_f = 3.5$ s.

study are simply linear Neumann (no flux or homogeneous) BCs, and they do not influence the order of convergence of the overall scheme. Therefore, this study verifies that the current approach to the treatment of the nonlinearity ψ, and its weighted averages appearing in the spatially discretized operator $\mathcal{L}_d$ in Equation (3.3), delivered

the desired second-order accuracy in space. Coupled with the Crank–Nicolson time-stepping's second-order accuracy in time, second order of convergence was expected to be seen in this refinement study.

As stated above, the exact self-similar solution to Equation (2.1) provided by Ciriello et al. [50] (and discussed in the Appendix) was evaluated at $t = t_0$ and mirrored about $x = 0$ as the IC. Upon evolving this IC numerically up to $t = t_f$, the numerical profile was compared to the same exact solution now evaluated at $t = t_f$. Hence, in accordance with the assumptions required to obtain this exact solution in [50], this first convergence study was limited to a uniform-width HS cell, i.e., $n = 0$.

Figure 4.1 shows the propagation of constant-mass viscous gravity current of three different fluids: (a) Newtonian, (b) shear-thinning and (c) shear-thickening power-law. The simulations indicate that currents propagate symmetrically about the center of the domain ($x = 0$). The sharp moving front $x_f(t)$ was accurately captured in these simulations on fairly modest (i.e., coarse) grids, without *any* signs of numerical instability or need for special treatment of the derivative discontinuity. The error was computed as a function of Δx during the grid refinement, and showed second-order convergence. This numerical example thus indicates that the proposed approach to treating the implicit nonlinear ψ terms, specifically their evaluation at $n+1/2$, is consistent with the desired second-order accuracy. The estimated order-of-convergence, calculated via Equation (4.3), is summarized in Table 4.2 for each of the above benchmarks. As expected, while convergence is observed in all three norms, the L^1 norm consistently exhibits second-order convergence across all cases.

It should be noted that the restriction on t_f, is necessary so that the current does not reach the domain boundaries, is critical since the chosen benchmark exact solution only describes the 'spreading' behavior of the current and not its 'levelling' (once it reaches the no-flux boundaries at $x = \pm L$). Indeed, the levelling regime possesses its distinct self-similar behavior (see, e.g., [54, 72]), which will be simulated and investigated in Section 5.4.2.

Table 4.2.
Estimated order-of-convergence $\mathfrak{p}$ for a 'centrally released' fixed fluid mass propagating in both directions in a uniform-width HS cell ($n = 0$) for the case of (a) a Newtonian fluid ($r = 1$), (b) a Shear-thinning fluid ($r = 0.7$), and (c) a Shear-thickening fluid ($r = 1.6$). Orders $\mathfrak{p}$ are evaluated between successive grid refinements via Equation (4.3), from the data shown in Figure 4.1.

Δx	$L^{\infty}_{\text{error}}$	order	L^{1}_{error}	order	L^{2}_{error}	order
7.5×10^{-3}	4.32×10^{-5}	–	1.38×10^{-6}	–	5.46×10^{-6}	–
3.75×10^{-3}	1.38×10^{-5}	1.64	4.37×10^{-7}	1.54	1.42×10^{-6}	1.94
1.875×10^{-3}	1.46×10^{-5}	0.78	9.78×10^{-8}	1.91	8.99×10^{-7}	1.30
9.375×10^{-4}	1.25×10^{-6}	1.70	1.47×10^{-8}	2.19	7.07×10^{-8}	2.09
4.6875×10^{-4}	1.32×10^{-6}	1.26	5.54×10^{-9}	1.99	4.21×10^{-8}	1.76

(a)

Δx	$L^{\infty}_{\text{error}}$	order	L^{1}_{error}	order	L^{2}_{error}	order
7.5×10^{-3}	5.01×10^{-6}	–	8.83×10^{-7}	–	1.39×10^{-6}	–
3.75×10^{-3}	1.39×10^{-5}	-1.47	2.26×10^{-7}	1.97	1.23×10^{-6}	1.76
1.875×10^{-3}	1.73×10^{-6}	0.77	3.86×10^{-8}	2.26	1.47×10^{-7}	1.62
9.375×10^{-4}	1.00×10^{-6}	0.77	1.06×10^{-8}	2.13	5.97×10^{-8}	1.51
4.6875×10^{-4}	8.23×10^{-7}	0.65	3.37×10^{-9}	2.01	2.91×10^{-8}	1.39

(b)

Δx	$L^{\infty}_{\text{error}}$	order	L^{1}_{error}	order	L^{2}_{error}	order
7.5×10^{-3}	2.12×10^{-4}	–	6.99×10^{-6}	–	2.69×10^{-5}	–
3.75×10^{-3}	3.36×10^{-5}	2.66	8.71×10^{-6}	3.00	3.73×10^{-6}	2.85
1.875×10^{-3}	1.72×10^{-5}	1.81	4.11×10^{-7}	2.04	1.39×10^{-6}	2.14
9.375×10^{-4}	1.05×10^{-5}	1.44	5.13×10^{-8}	2.36	5.10×10^{-7}	1.91
4.6875×10^{-4}	6.64×10^{-6}	1.25	1.97×10^{-8}	2.12	2.13×10^{-7}	1.75

(c)

4.1.2 Propagation of a Fixed Mass of Fluid in a Single Direction

To ascertain the accuracy of the discretization of the nonlinear BCs, a one-sided domain $x \in [\ell, L]$ with $\ell = 0$ was considered once again. For the case of the current spreading away from the origin, the BC at the 'left' end of the domain (from which the fluid is released) is now non-trivial, and its proper discretization is key to the overall order of the convergence of the scheme. Conveniently, for a fixed mass ($\alpha = 0$), the BCs still reduce to homogeneous Neumann conditions (recall Section 3.3), however, h is no longer zero at the boundary (as was the case in Section 4.1.1). Now, this successively 'more complicated' case was benchmarked.

Once again it was ensured that t_f was such that the current did not reach the downstream ($x = L$) domain end. Then, similar to Section 4.1.1, the exact solution of Ciriello et al. [50] was used as the benchmark exact solution; again, this required restricting to uniform-width HS cells (i.e., $n = 0$).

Figure 4.2 and the accompanying Table 4.3 show second-order estimated rate-of-convergence in the L^1 norm. This result indicates that the decision to implement the scheme on a staggered grid, in which case the Neumann BCs (for $\alpha = 0$) are conveniently discretized using two-point central differences at the boundary, is indeed the correct decision. Indeed, for the case of a Newtonian fluid, there is little to no variations in the values of the three norms of the error for the current spreading centrally in two directions versus in only one direction.

4.1.3 Propagation in a Single Direction with Mass Injection

Finally, the numerical scheme was subjected to its most stringent test yet. That is, the estimated order of convergence under mass injection conditions ($\alpha \neq 0$) was computed. The injection occurs near the cell's origin while the current propagates away from this location. Since $\alpha \neq 0$, the fully nonlinear forms of the BCs as given in Equations (2.5) and (2.7) now come into play.

Table 4.3.
Estimated order-of-convergence for a fixed fluid mass propagating in a single direction in a uniform-width HS cell ($n = 0$) for the case of (a) a Newtonian fluid ($r = 1$), (b) a Shear-thinning fluid ($r = 0.5$), and (c) a Shear-thickening fluid ($r = 1.5$). Orders $\mathfrak{p}$ are evaluated between successive grid refinements via Equation (4.3), from the data shown in Figure 4.2.

Δx	$L^{\infty}_{\text{error}}$	order	L^{1}_{error}	order	L^{2}_{error}	order
7.5×10^{-3}	4.32×10^{-5}	–	6.84×10^{-7}	–	3.86×10^{-6}	–
3.75×10^{-3}	1.38×10^{-5}	1.64	2.36×10^{-7}	1.53	1.00×10^{-6}	1.87
1.875×10^{-3}	1.46×10^{-5}	0.78	4.88×10^{-8}	1.90	6.36×10^{-7}	1.27
9.375×10^{-4}	1.25×10^{-6}	1.70	7.32×10^{-9}	2.18	5.00×10^{-8}	2.07
4.6875×10^{-4}	1.32×10^{-6}	1.26	2.77×10^{-9}	1.99	2.97×10^{-8}	1.74

(a)

Δx	$L^{\infty}_{\text{error}}$	order	L^{1}_{error}	order	L^{2}_{error}	order
7.5×10^{-3}	9.03×10^{-6}	–	2.98×10^{-7}	–	9.27×10^{-7}	–
3.75×10^{-3}	3.93×10^{-6}	1.20	5.66×10^{-8}	2.40	2.90×10^{-7}	1.68
1.875×10^{-3}	2.30×10^{-6}	0.99	1.78×10^{-8}	2.03	1.24×10^{-7}	1.45
9.375×10^{-4}	8.58×10^{-7}	1.13	4.81×10^{-9}	1.98	2.85×10^{-8}	1.67
4.6875×10^{-4}	5.08×10^{-7}	1.04	1.01×10^{-9}	2.05	1.41×10^{-8}	1.51

(b)

Δx	$L^{\infty}_{\text{error}}$	order	L^{1}_{error}	order	L^{2}_{error}	order
7.5×10^{-3}	4.35×10^{-5}	–	1.15×10^{-6}	–	5.37×10^{-6}	–
3.75×10^{-3}	2.15×10^{-5}	1.02	6.25×10^{-7}	0.88	2.17×10^{-6}	1.31
1.875×10^{-3}	1.18×10^{-5}	0.94	7.09×10^{-8}	2.01	7.22×10^{-7}	1.45
9.375×10^{-4}	5.96×10^{-6}	0.96	2.66×10^{-8}	1.81	2.57×10^{-7}	1.46
4.6875×10^{-4}	3.22×10^{-6}	0.94	1.13×10^{-8}	1.67	9.31×10^{-8}	1.46

(c)

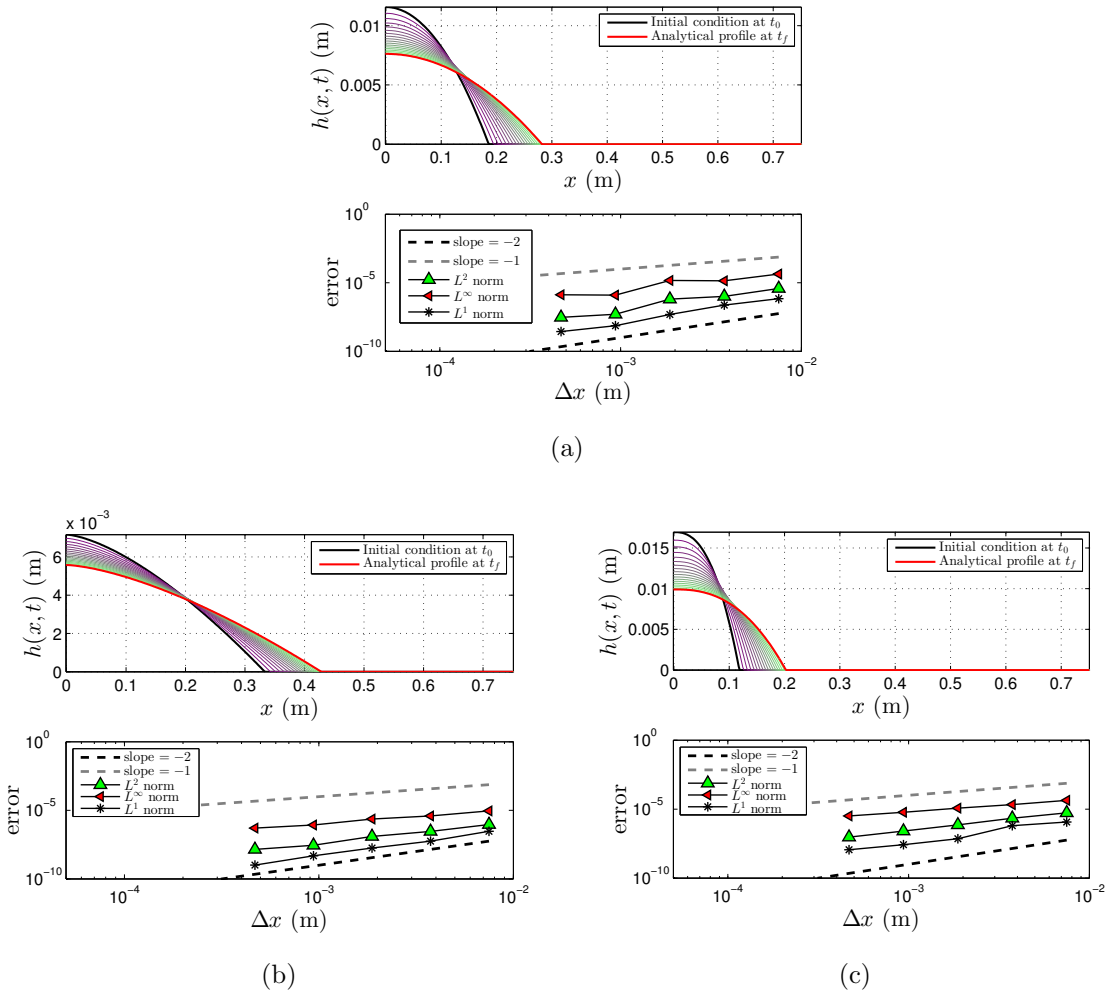

Fig. 4.2. Estimated order-of-convergence study for the release of a fixed fluid mass propagating in a single direction (away from cell's origin) in a uniform-width HS cell ($n = 0$) for the case of (a) a Newtonian fluid ($r = 1$), (b) a Shear-thinning fluid ($r = 0.5$), and (c) a Shear-thickening fluid ($r = 1.5$). Once again, the currents were released at $t_0 = 1$ s and spread until $t_f = 3.5$ s. The currents' shapes are plotted from early times (purple/dark) through late times (green/light). The remaining model parameters for these simulations are the same as in Figure 4.1.

Unlike the previously discussed cases of the release of a fixed fluid mass, a straightforward exact solution to the nonlinear ODE emerging from the self-similar analysis is not available. For a variable mass, obtaining a benchmark solution from the self-

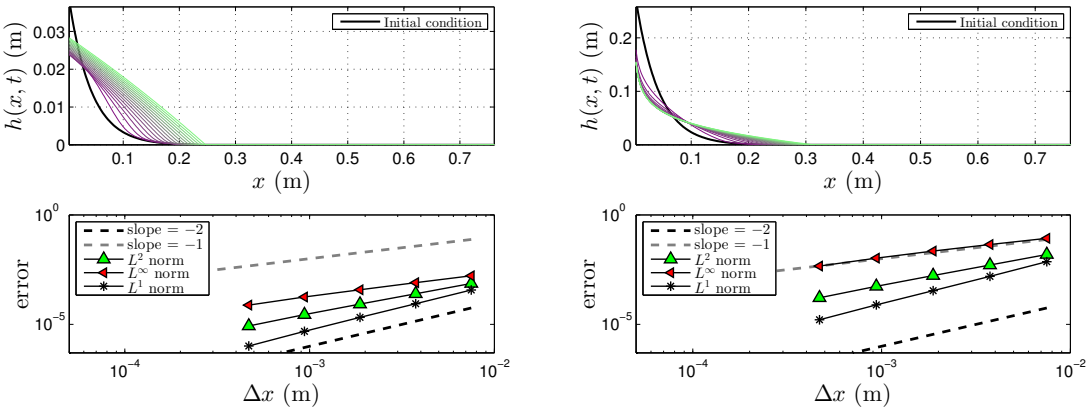

(a) (b)

Fig. 4.3. Estimated order-of-convergence study for a variable-mass gravity current with injection at $x = \ell$ on the truncated domain $x \in [\ell, L]$ with $\ell = \Delta x_0$. Simulations are shown for the case of (a) a Newtonian fluid in a uniform-width HS cell ($r = 1$, $n = 0$) with injection exponent $\alpha = 1$, and (b) a shear-thickening fluid in a variable width cell ($r = 0.6$, $n = 0.6$) with injection exponent $\alpha = 1.5$. The remaining model parameters for these simulations were the same as in Figure 4.1.

similar analysis is significantly more challenging, given that the nonlinear ODE had be solved *numerically* (see the Appendix). Despite the availability of accurate stiff ODE solvers, such as `ode15s` in MATLAB, it is quite difficult to map the numerical solution of the self-similar ODE onto the selected computational grid, while maintaining the desired order of accuracy throughout this procedure. Therefore, in this numerical study, it was easier to use a 'fine-grid' numerical solution as the benchmark solution. This benchmark solution was then compared against the solutions on successively coarser grids to establish the estimated order of convergence of the numerical scheme.

For this study, the simulation domain is $x \in [\ell, L]$ with $\ell = \Delta x_0$, so that $x_{i=0} = \ell - \Delta x_0/2$ and $x_{i=N} = L + \Delta x_0/2$, and the boundary points are at the same cell faces on all grids during the refinement. The IC at $t_0 = 0$ s is the one given in Equation (2.9)

with $a = 0.001$, $b = 0.35$, $c = 25$. The solution was advanced numerically up to $t_f = 1.5$ s.

Figure 4.3 and the accompanying Table 4.4 show that the order of convergence of the numerical method is second order in space and time in the L^1 norm, as expected. In this figure, to show some variety, two distinct but arbitrarily selected cases were simulated: (a) a Newtonian fluid in a uniform-width HS cell ($n = 0$) with volume growth exponent $\alpha = 1$, and (b) a non-Newtonian (shear-thinning, $r = 0.6$) fluid in a shaped HS cell (width exponent $n = 0.6$) with the volume growth exponent $\alpha = 1.5$. Second-order convergence was observed in both cases.

With this final numerical test, the formal truncation error of the proposed numerical scheme is justified. This result is nontrivial because the PDE and the scheme are both *nonlinear*, requiring subtle approximation on a staggered grid, across half-time steps, and linearization of algebraic system via internal iterations.

4.2 Satisfaction of the Mass Constraint at the Discrete Level

Since the BCs derived in Section 2.2 (and discretized in Section 3.3) stem from the mass conservation constraint (i.e., Equation (2.2) or Equation (2.3)), it is expected that the proposed finite-difference scheme should produce a solution $h(x,t)$ that satisfies Equation (2.2) or Equation (2.3) to within $\mathcal{O}\left[(\Delta x)^2 + (\Delta t)^2\right]$ or better, if this constraint is checked independently again after computing the numerical solution. To verify this capability of the scheme, in this section, two cases are considered: (i) a fixed fluid mass released near the origin ($\alpha = 0$), and (ii) spreading subject to mass injection ($\alpha > 0$) near the origin. Both cases were studied on the domain $x \in [\ell, L]$ with $\ell = \Delta x$. The solution was evolved on the time interval $t \in (t_0, t_f]$, and the volume error for each t was computed as

$$\left| \int_{\ell}^{L} h(x,t) b(x) \, \mathrm{d}x - (\mathcal{V}_0 + \mathcal{V}_{\mathrm{in}} t^{\alpha}) \right|, \tag{4.4}$$

where the x-integration was performed by the trapezoidal rule to $\mathcal{O}\left[(\Delta x)^2\right]$ on the staggered mesh, as before. It was expected that the volume error, as defined in Equa-

Table 4.4.
Estimated order-of-convergence for a variable-mass gravity current propagating in a single direction with injection at the origin of the HS cell. Orders $\mathfrak{p}$ are evaluated between successive grid refinements via Equation (4.3), from the data shown in Figure 4.3. Orders are tabulated for the case of (a) a Newtonian fluid in a uniform-width HS cell ($r = 1$, $n = 0$) with injection exponent $\alpha = 1$, and (b) a shear-thickening fluid in a variable width cell ($r = 0.6$, $n = 0.6$) with injection exponent $\alpha = 1.5$.

Δx	$L^{\infty}_{\text{error}}$	order	L^{1}_{error}	order	L^{2}_{error}	order
7.5×10^{-3}	1.63×10^{-3}	–	3.71×10^{-4}	–	7.41×10^{-4}	–
3.75×10^{-3}	7.98×10^{-4}	1.06	8.77×10^{-5}	2.08	2.50×10^{-4}	1.57
1.875×10^{-3}	3.82×10^{-4}	1.06	2.07×10^{-5}	2.08	8.44×10^{-5}	1.57
9.375×10^{-4}	1.78×10^{-4}	1.07	4.81×10^{-6}	2.09	2.77×10^{-5}	1.58
4.6875×10^{-4}	7.60×10^{-5}	1.11	1.03×10^{-6}	2.12	8.39×10^{-6}	1.61

(a)

Δx	$L^{\infty}_{\text{error}}$	order	L^{1}_{error}	order	L^{2}_{error}	order
7.5×10^{-3}	8.55×10^{-2}	–	7.27×10^{-3}	–	1.56×10^{-2}	–
3.75×10^{-3}	4.45×10^{-2}	0.94	1.56×10^{-3}	2.22	5.12×10^{-3}	1.60
1.875×10^{-3}	2.23×10^{-2}	0.97	3.47×10^{-4}	2.20	1.69×10^{-3}	1.60
9.375×10^{-4}	1.06×10^{-2}	1.00	7.74×10^{-5}	2.18	5.45×10^{-4}	1.61
4.6875×10^{-4}	4.95×10^{-3}	1.05	1.62×10^{-5}	2.20	1.63×10^{-4}	1.64

(b)

tion (4.4), was $\mathcal{O}\left[(\Delta x)^2 + (\Delta t)^2\right]$, the same as the overall scheme. In this numerical study, the selection of the IC is no longer critical, as there is no comparison with an exact self-similar solution. Accordingly, generic ICs from Equations (2.8) and (2.9) were selected.

4.2.1 Fixed Mass Release ($\alpha = 0$)

In this case, the IC was a cubic polynomial determined from Equation (2.8) with $\gamma = 3$, $x_0 = 0.25$ m. The error in the total fluid volume as a function of t was compared with the initial one. Figure 4.4 shows that, while numerical error did build up in the total volume, the initial volume remained conserved to within (or better than) $(\Delta t)^2 = 10^{-6}$.

4.2.2 Mass Injection ($\alpha > 0$)

A more stringent test of conservation properties of the proposed scheme was conducted by applying the nonlinear BC associated with imposed mass injection at one end. For this case, the IC was taken to be the function in Equation (2.9) with $a = 0.001$ m, $b = 0.35$ m and $c = 25$ m^{-1} and $x_0 = \frac{1}{c} \ln \frac{a}{b}$. A combination of n, r and α values were considered to highlight the conservation properties across different physical regimes. Figure 4.5 shows that, in all cases, the volume constraint was properly respected; while the volume error built up, it remained small (within or better than $(\Delta t)^2 = 10^{-6}$).

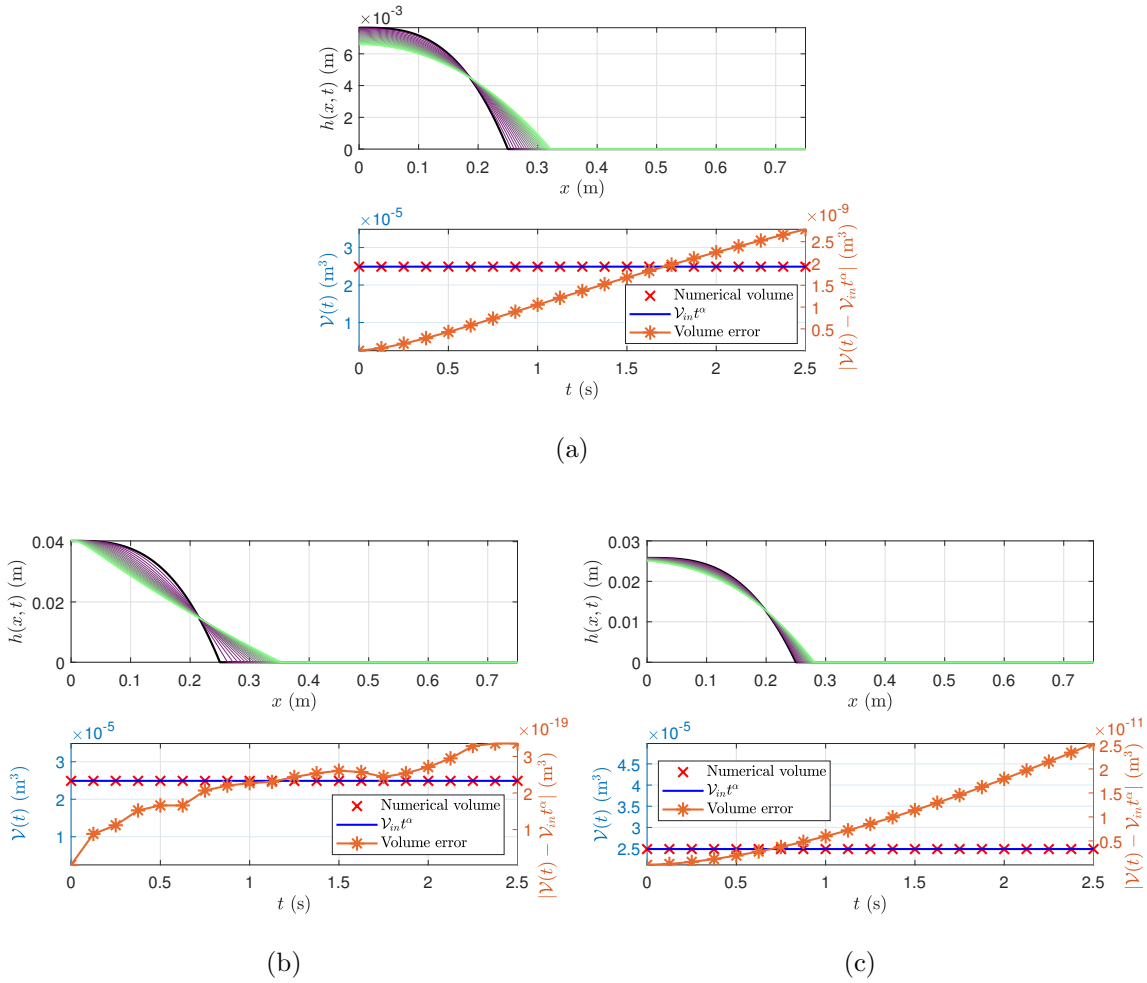

Fig. 4.4. Results of the conservation study for the release of a fixed fluid mass. To highlight the scheme's capabilities, each case features a different combination of a power-law non-Newtonian fluid (r) and HS cell (n): (a) $r = 1, n = 0$, (b) $r = 0.7, n = 0.7$, and (c) $r = 1.5, n = 0.5$. The currents were allowed to propagate from $t_0 = 0$ s up to $t_f = 2.5$ s, through 2500 time steps ($\Rightarrow \Delta t = 10^{-3}$ s). In all cases, $\alpha = 0$ and $\mathcal{V}_0 = \mathcal{V}_{\text{in}} = 2.4902 \times 10^{-5}$ m^3. The remaining model parameters for these simulations are the same as in Figure 4.1.

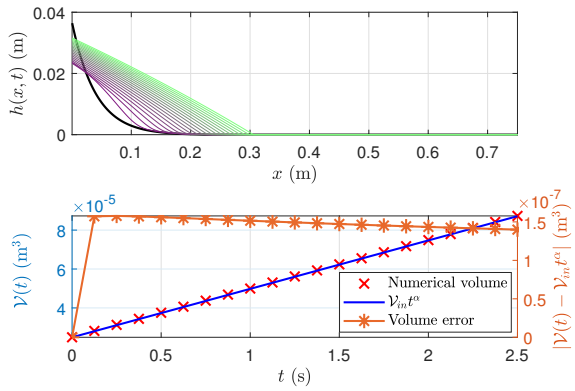

(a)

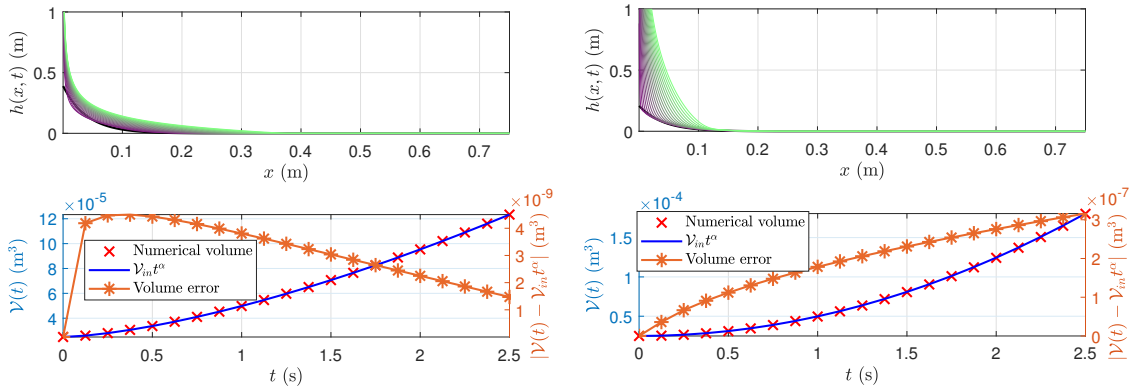

(b) (c)

Fig. 4.5. Results of the conservation study for mass injection. The volume exponent α was varied through three separate cases: (a) $\alpha = 1$ for a Newtonian fluid in uniform HS cell ($r = 1, n = 0$), (b) $\alpha = 1.5$ for a shear-thinning fluid in a variable width HS cell ($r = 0.7$, $n = 0.7$), and (c) $\alpha = 2$ for a shear-thickening fluid in a variable width HS cell ($r = 1.5$, $n = 0.5$). In all cases, $\mathcal{V}_{\text{in}}$, t_0, t_f, Δt are as in Figure 4.4. The remaining model parameters for these simulations are the same as in Figure 4.1.

5. SECOND-KIND SELF-SIMILARITY DURING SPREADING AND LEVELING OF GRAVITY CURRENTS IN SHAPED HELE-SHAW CELLS

Having established the convergence and conservation properties of the proposed implicit, finite-difference scheme in Chapter 4, there is now an accurate numerical tool with low computational overhead that can be used to study second-kind self-similarity of viscous gravity current propagation. Specifically, of interest in the below discussion is the case of the release of a fixed mass of Newtonian fluid. After being released at a finite distance x_0 away from the origin (i.e., $x_f(t = 0) = x_0$) in a variable-width HS cell, the fluid spreads towards the channel origin as shown in Figure 5.1. In this case, the emergence of an an extra length scale, x_0 (in addition to the channel length, L, where now $\ell = 0$) complicates the dimensional analysis of the flow. This chapter is dedicated to the development of the nonlinear eigenvalue problem emerging in the analytical treatment of flows of this type, and the use of the numerical scheme from Chapter 3 to understand the possible second-kind self-similar behaviors and further elucidate previous experimental data.

5.1 Flow Domain and Characteristics

For the purposes of this chapter, the flow domain is a Hele-Shaw (HS) cell of variable width in the x-direction. As before, the width of the HS cell is defined by a power-law in x, i.e., $b(x) = b_1 x^n$ with $b_1 > 0$ and $n \in (0, 1)$ being constant. The HS cell is assumed to be either completely porous ($\phi = 1$) or have a constant porosity ($\phi = const.$), which could be absorbed into the definition of the width function. The HS cell is vertically unconfined and possesses an impermeable bottom surface. Additionally, to compare with available experiments, the fluid is restricted to be

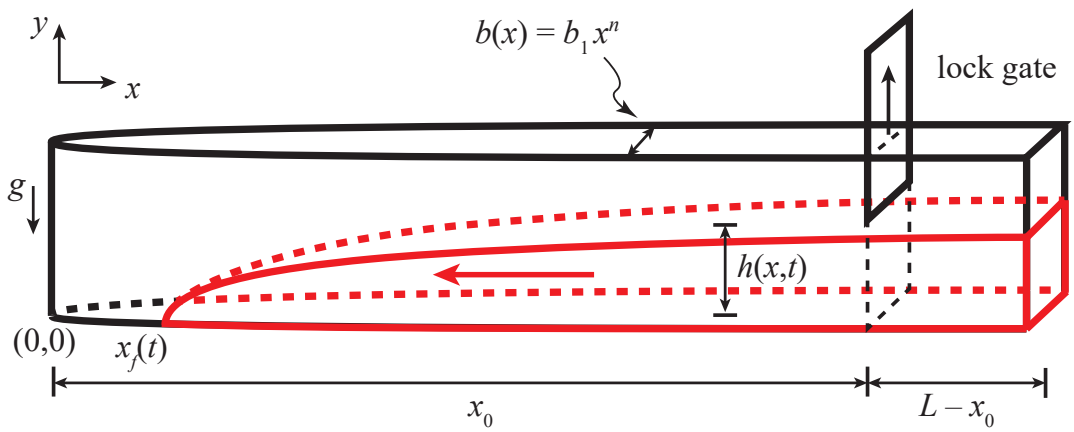

Fig. 5.1. Flow geometry associated with the study of a Newtonian fluid ($r = 1$) in a variable-width HS cell. The location of lock gate, $x = x_0$, introduces an additional length scale into the mathematical model. The HS cell is considered to be completely porous medium (i.e., $\phi = 1$). Figure reproduced and adapted with permission from [Zheng et al., Influence of heterogeneity on second-kind self-similar solutions for viscous gravity currents, J. Fluid Mech., vol. 747, p. 221] © Cambridge University Press 2014.

Newtonian ($r = 1$). Accordingly, the dimensionless exponents p and q appearing in the governing PDE (2.1) simplify to $p = n$, $q = 3n$ (recall Table 2.2); this definition of the exponents is directly inserted into the below mathematical model. Finally, the fluid volume is kept constant, with no mass injection imposed at the boundaries, i.e., $\mathcal{V}(t) = \mathcal{V}_{in} = const.$

In line with experiments supplementing the discussion in this chapter, the fluid is assumed to be initially contained behind a release- or lock-gate located at $x = x_0$. As depicted in Figure 5.1, upon opening the gate, the current immediately slumps and begins to spread 'leftwards', in direction of the origin at $x = 0$ m, where the width vanishes ($b(0) = 0$). Therefore, the nose of the current is initially at $x_f(0) = x_0$. The current spreads until it reaches the origin at a time of 'closure', $t = t_c$ (also termed 'touch-down' time in prior literature [38]); this period $t \in [0, t_c]$) is hereafter termed

'pre-closure'. Thereafter, the current levels at $x = 0$ until $h(x, t \to \infty) = const.$; this period $t \in [t_c, \infty)$ is hereafter referred to as 'post-closure'.

5.2 Mathematical Model

The closure time t_c can be determined numerically using the scheme developed and benchmarked in previous chapters, or it can be obtained from experiments. This additional time scale can be *infinite*, if the current never reaches the origin, but for the present purposes it is assumed that t_c if finite for reasons made clear below. Regardless, t_c, or equivalently x_0, emerge as a extra time, or length, scale that makes the use of of a scaling analysis alone to obtain a self-similar solution ambiguous. For example, x_0 now appears in the global mass conservation constraint Equation (2.3), which is must be implemented over the portion of the domain behind the lock-gate, i.e., $x \in [x_0, L]$. Indeed, it is no longer that *complete* self-similarity with respect to a single similarity variable can be observed [23]. Nevertheless, should *any* self-similar behavior be expected or observed? The answer is 'yes'. In this situation, the phase-plane formalism can be used to obtain the latter answer; see, e.g., Gratton and Minotti's [51] application of this method, which is lucidly explained in the classical book by Sedov [73]. The resulting analysis of the governing equations in an appropriate phase plane can predict the existence of *two* self-similar regimes, one in pre- and one in post-closure. It is expected that any self-similarity variable would explicitly feature t_c or x_0. It is the goal of this chapter to confirm these theoretical predictions.

Regardless of the questions arising regarding the scaling analysis, the governing thin-film equation (2.1) introduced in Section 2.2, in which the right-hand side corresponds a fluid flux re-expressed in terms of the gradient of the fluid interface's shape ($\partial h/\partial x$) remains valid. For the situation in Figure 5.1, the nonlinearity conveniently reduces to $\psi(h) = h$ (recall Table 2.2). To apply the phase-plane analysis idea [51], it is convenient to follow [38] (see also, e.g., [54]) and first re-write the governing equation, which is second-order in x, as a system of two first-order equations. This

mathematical manipulation has physical significance. Under the lubrication approximation, the pressure distribution was hydrostatic and Darcy's law and the continuity equation take the form

$$u = -Ax^{2n}\frac{\partial h}{\partial x}, \tag{5.1a}$$

$$\frac{\partial h}{\partial t} + \frac{1}{x^n}\frac{\partial}{\partial x}(x^n hu) = 0, \tag{5.1b}$$

where the constant $A = (\Delta\rho g b_1^2)/(12\mu_0)$ retains its definition from Table 2.2, and u is the Darcy ('superficial') velocity. Obviously, Equation (5.1a) can substituted into Equation (5.1b) to yield the PDE (2.1) introduced in Section 2.2.

Assuming that $t_c < \infty$, a shifted time $\tau = t_c - t$ is introduced. This shifted time represents the time left for the current to reach the origin, and its definition necessitates the use of numerical simulations (or experiments) to determine the closure time t_c *a priori*. (In the case that $t_c \to \infty$, τ becomes indeterminate, and the transformation and subsequent phase plane analysis become invalid. Of course, the case of $t_c < \infty$ is the most interesting one, and it allows for a discussion of both spreading and leveling of the flow.) The next step in the phase-plane formalism is to render Equations (5.1a) and (5.1b) dimensionless by using the *independent variables as dimensional scales*. Specifically, through the transformations

$$u(x,t) = \frac{x}{\tau}U(x,\tau), \tag{5.2a}$$

$$h(x,t) = \frac{1}{A}\frac{x^{2(1-n)}}{\tau}H(x,\tau), \tag{5.2b}$$

the quantities $U(x,\tau)$ and $H(x,\tau)$ become the dimensionless analogs to the Darcy velocity and current height, respectively. Note that since, $u \leq 0$ for the current moving towards origin, $U \leq 0$ as well, while $H \geq 0$ for the equal and opposite reason.

Substituting Equations (5.2a) and (5.2b) into Equations (5.1a) and (5.1b), the governing equations are re-written in terms of H and U (see [38]):

$$x\frac{\partial H}{\partial x} + 2(1-n)H + U = 0, \tag{5.3a}$$

$$\tau\frac{\partial H}{\partial \tau} - H - x\frac{\partial}{\partial x}(HU) - (3-n)HU = 0. \tag{5.3b}$$

Anticipating a self-similar solution, a *second-kind* self-similar variable of the form $\xi = x/\tau^{\delta}$ is introduced (not to be mistaken with the first-kind similarity variable η emerging from scaling analysis which was discussed previously in Section 1 and the Appendix A). Critically, δ is *unknown* here, and ξ explicitly features t_c through τ. The assumption of self-similarity now necessitates that $H = H(\xi)$ and $U = U(\xi)$. This allows the governing Equations (5.3) to be reduced to a system of one-way coupled ODEs:

$$\frac{\mathrm{d}U}{\mathrm{d}H} = \frac{H[(n+1)U - 2(1-n)\delta + 1] - U(U+\delta)}{H[2(1-n)H + U]}, \tag{5.4a}$$

$$\frac{\mathrm{d}\ln|\xi|}{\mathrm{d}H} = -\frac{1}{U + 2(1-n)H}. \tag{5.4b}$$

Equations (5.4a) represents an autonomous ODE for $U(H)$ depending on a parameter δ. Once $U(H)$ is known, then Equation (5.4b) is used to find $\xi(H)$, from which the the self-similar profiles $H(\xi)$ and $U(\xi)$ can be reconstituted from $U(H)$ (i.e., 're-parameterized' in terms of ξ). However, before any of these ODEs can be solved, a suitable set of BCs must be specified. Note that the success of the self-similar transformation to arrive at the system of Equations (5.4) already suggests that a self-similar solution might exist. However, since δ is unknown, the problem becomes an *eigenvalue problem*. With a suitable set of BCs, it is expected that both $U(H)$ and δ emerge as an 'eigenpair' solution to Equation (5.4a).

Since Equation (5.4a) is a planar ODE, it follows that BCs arise as beginning and endpoints of integral curves in the (H, U) plane. In order to identify the integral curves of physical significance in this (H, U) space, i.e., those solutions $U(H)$ that correspond to an observable self-similar behaviour, care must be taken. To identify the potentially meaningful integral curves, first the ODE's critical points in the phase plane must be found. Following [38, 51], critical points are found by setting the numerator and denominator in Equation (5.4a) to 0 simultaneously. Thus, the points

denoted below as O, A and B are obtained. The final critical point D is obtained by setting the denominator in Equation (5.4a) to ∞. In summary:

$$\text{O} \ : \ (H, U) = (0, 0), \tag{5.5a}$$

$$\text{A} \ : \ (H, U) = (0, -\delta), \tag{5.5b}$$

$$\text{B} \ : \ (H, U) = \left(\frac{1}{2(1-n)(3-n)} \, , \, -\frac{1}{3-n} \right), \tag{5.5c}$$

$$\text{D} \ : \ (H, U) = \left(-\infty, \frac{2(1-n)\delta - 1}{n+1} \right). \tag{5.5d}$$

Points A and D are a function of the eigenvalue δ, showing how the BCs will 'conspire' with the ODE to determine the appropriate eigenpair solution.

As described in [38], point O corresponded to the instant at which the current reached the point of zero permeability (i.e., the point of 'closure' at the channel's origin, corresponding to $x = 0$ or $\xi = 0$). Meanwhile, point A corresponded to the moving front of a spreading current (at $x = x_f(t)$ or $\xi = \xi_N$). Point B does not have a physical interpretation in the present context. Point D corresponded to the leveling (post-closure) behavior. The integral curves connecting O and A, and D and O in a phase plane thus represent the sought self-similar solutions to the problem during the pre-closure ($t < t_c$) and post-closure ($t > t_c$) regimes. Having identified the integral curves of interest, the task of finding a self-similar solution has been reduced to a nonlinear eigenvalue problem. Specifically, the question now is, given n, what value(s) of δ allow for the existence of phase-plane curves that connect point O to A and point D to O. The nonlinear eigenvalue problem can be solved using a 'shooting' procedure (for details see, [38, Section 2.1.2] or [51]). For instance, for the case of $n = 0.5$, the value of δ was identified to single precision as $\delta \simeq 1.542269$. The corresponding phase-plane is depicted in Figure 5.2, verifying the existence of the sought-after solutions.

In this manner, the existence of two distinct self-similar regimes was conclusively proved and value of exponent δ was determined. To proceed with the current analysis, it was desired to obtain the analytical height function $H(\xi)$ which could then be

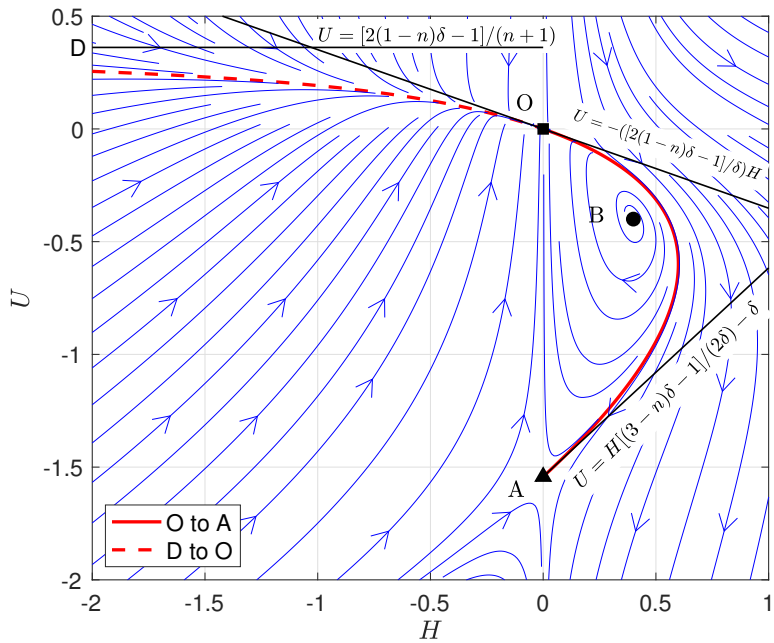

Fig. 5.2. Phase-plane portrait of the ODE (5.4a) describing the self-similar propagation of a Newtonian current in a shaped HS cell with width exponent $n = 0.5$. The eigenvalue δ appearing in the definition of the similarity variable ξ was calculated to be $1.542269\ldots$. The integral curves OA (solid) and DO (dashed) represent self-similar pre- and post-closure solutions, respectively.

compared with numerical and experimental data. To derive this profile, both Equations (5.4a) and (5.4b) were broken into a system of ODEs. This system was subject to the BCs defined in Figure 5.2 in the form of the slopes at the critical points.

It is inconvenient to go back and solve Equation (5.4b) for $\xi(U)$, after solving Equation (5.4a), and re-parametrizing $U(\xi)$ and $H(\xi)$. A mathematical 'trick' can be used to avoid this inconvenience. First, the similarity variable ξ is scaled by its value at the nose, i.e., ξ_N (denoted by ξ_f in [38]), then the channel origin is defined as the point at which $\xi/\xi_N = 0$ and the moving front of the current is at $\xi/\xi_N = 1$. Then, after some algebra, it is possible to rewrite Equations (5.4) as

$$\frac{\mathrm{d}}{\mathrm{d}\ln|\xi/\xi_N|}\begin{Bmatrix} H \\ U \end{Bmatrix} = \begin{Bmatrix} -[2(1-n)H + U] \\ \big(-H[(n+1)U - 2(1-n)\delta + 1] + U(U+\delta)\big)/H \end{Bmatrix}, \quad (5.6)$$

where $\delta \approx 1.5423$ for $n = 0.5$ is already known. An analogous system of ODEs can be derived for the case of the propagation of a power-law non-Newtonian fluid in a variable-width Hele-Shaw cell [61]:

$$\frac{\mathrm{d}}{\mathrm{d}\ln|\xi/\xi_N|}\begin{Bmatrix} H \\ U \end{Bmatrix} = \begin{Bmatrix} -[(r+1)(1-n)H + U|U|^{r-1}] \\ \big(-H[(n+1)U - (r+1)(1-n)\delta + 1] + U|U|^{r-1}(U+\delta)\big)/H \end{Bmatrix}. \quad (5.7)$$

Similar to Equations (5.5), a set of critical points for the above ODE system can be derived to determine integral curves of physical importance in the corresponding phase plane. The critical points carry the same physical meanings as described previously, but they are now given by

$$\mathrm{O} \ : \ (H, U) = (0, 0), \quad (5.8a)$$

$$\mathrm{A} \ : \ (H, U) = (0, -\delta), \quad (5.8b)$$

$$\mathrm{D} \ : \ (H, U) = \left(-\infty, \frac{(1+r)(1-n)\delta - 1}{n+1}\right). \quad (5.8c)$$

The autonomous systems of ODEs (5.6) or (5.7) can be solved using a shooting method, e.g., as described above (see also Appendix A).

Returning to the specific case of a Newtonian fluid ($r = 1$), for pre-closure, a small perturbation is introduced to point A by taking $H|_{\mathrm{A}} = 10^{-3}$, while the scaled velocity is initialized using the linearization of the ODE at A as $U|_{\mathrm{A}} = H|_{\mathrm{A}} \cdot [(3 - n)\delta - 1]/(2\delta) - \delta$ via Equation (5.5b). Equation (5.6) is then be solved by shooting 'backwards' from A to O, using a stiff numerical integration algorithm (e.g., `ode15s` in MATLAB). Likewise, the post-closure solution is obtained by initializing the solution at O: $H|_{\mathrm{O}} = 10^{-3}$ was the small perturbation and using the linearization of the ODE to set $U|_{\mathrm{O}} = -H|_{\mathrm{A}} \cdot [2(1-n)\delta - 1]/\delta$.

At this point in the analysis, a self-similar solution to the governing PDE has been obtained, albeit numerically. However, any additional analysis and interpretation of this solution requires rescaling back to the physical variables, which require the

Table 5.1.
A summary of experimental parameters for a 95% glycerol-water mixture at 20°C used as the working fluid.

Quantity	Value	Units
Channel length L	0.75	m
Lock-gate location x_0	0.4897	m
Width coefficient b_1	0.01732	m^{1-n}
Width exponent n	0.5	–
Total released mass w	0.3155	kg
Density ρ	1250.8	$\mathrm{kg/m^3}$
Dynamic viscosity μ_0	0.62119	Pa·s

explicit knowledge of at least t_c and a 'pre-factor' b, which is discussed in detail in below sections. Therefore, the goal now is to determine these quantities using the proposed finite-difference scheme, and to ascertain the physical validity of the second-kind self-similar solution obtained from phase-plane analysis in this section.

5.3 Experimental Study of a 95% Glycerol-Water Mixture in a Converging Hele-Shaw Cell

An experiment replicating the flow depicted in Figure 5.1 was performed with a 95% glycerol-water mixture in a horizontal HS cell of variable width by Zhong Zheng (see also discussion in [38]). The experiment was conducted at 20°C, and the corresponding fluid properties were determined using standard fits in [70, 71]. A summary of the geometrical parameters and fluid properties necessary to analyze the experiments are given in Table 5.1.

A constant volume of the mixture, which is assumed to behave as a Newtonian fluid ($r = 1$) was released from behind a lock-gate gate and allowed to spread towards the origin of the horizontal HS cell having a width exponent $n = 0.5$. As described

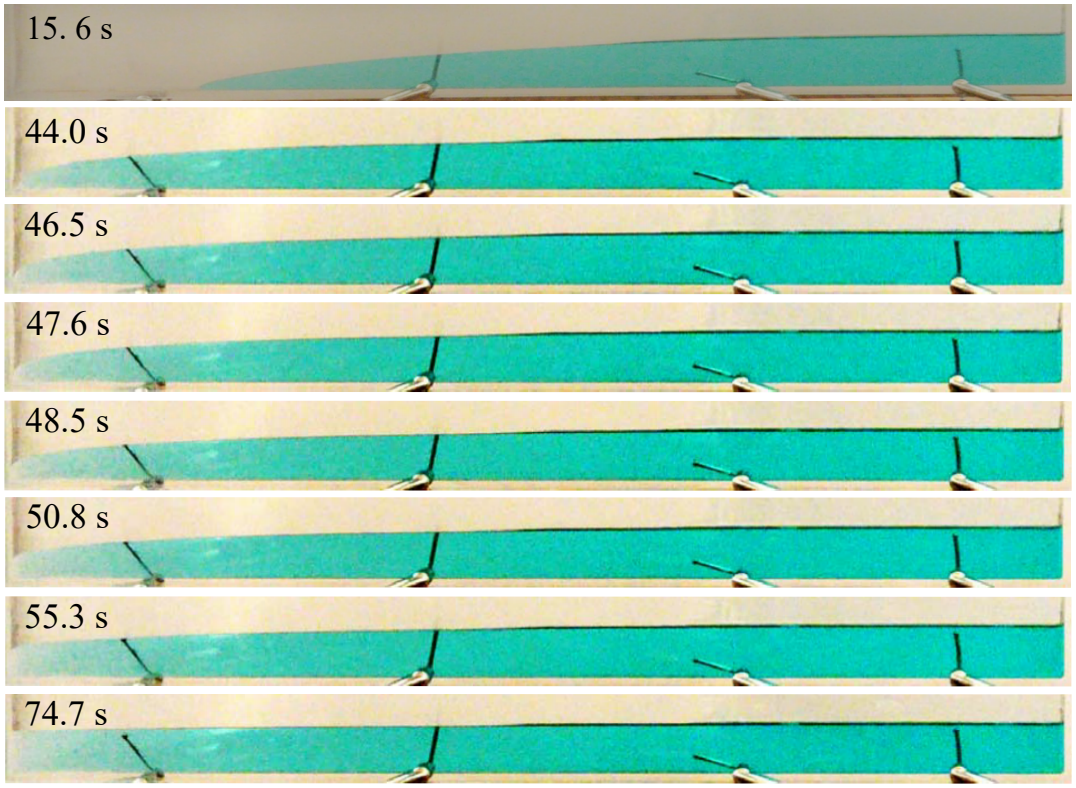

Fig. 5.3. Experimental time-lapse of a gravity current profile $h(x,t)$ leveling in a variable-gap Hele-Shaw cell. A 95% glycerol-water at 20°C was released into the cell and photographed during the pre- and post-closure. The cell was of length $L = 0.75$ m, and the release gate was located at $x_0 = 0.4897$ m. Per experiments, $t_c \approx 44.03$ s, so most of the shown time-lapse represents the leveling process. (Unpublished figure courtesy of Dr. Zhong Zheng, used and adapted with permission.)

in [38, Section 3], the shape of the current was photographed intermittently using a USB camera, yielding some example profiles shown in Figure 5.3. The fluid was colored blue using food dye to make its digital post-processing convenient. The lock-gate's location x_0 was kept comparable to the length of the cell L to provide a longer distance over which the current's spreading behavior could be observed. Additionally, it was assumed that given a longer period of time to spread, the current would have forgotten its initial condition (its 'boxy' shape as it sat behind the lock-gate for $t \leq 0$)

and entered its pre-closure self-similar regime as $t \to t_c$ (or $\tau \to 0^+$). (This notion of 'loss of memory' and how it relates to the concept of self-similarity is discussed in more detail in Section 5.4.) Obtaining accurate experimental data of the current as it approaches the origin becomes challenging as the flow is accelerated in accordance with the transversely converging nature of the HS cell. Nevertheless, experiments suggest that the current's closure time (i.e., the time it takes to the reach $x_f(t_c) = 0$ from $x_f(0) = x_0$) is $t_c \approx 44.03$ s. Thereafter, the current entered the leveling, or post-closure, regime.

Before we can apply any theory based on Equation (2.1), it is critical to ensure that the experiments fall within the assumptions the lubrication approximation, i.e., the reduced Reynolds number (defined as the product of the transverse aspect ratio and Reynolds number) has to be small. Assuming the streamwise length scale to be x_0, the transverse length scale is $b_1 x_0^n$. The velocity scale is then simply taken to be x_0/t_c. The lubrication approximation requires that $Re = (\rho b_1^2 x_0^{2n})/(\mu_0 t_c)$ is small, i.e., $Re \ll 1$. For the experiments conducted in accordance with the parameters in Table (5.1), one can conclude that $Re \approx 6.7 \times 10^{-3}$, ensuring that the lubrication approximation is valid.

Figure 5.3 shows a series of current profiles. The height of the current $h(x,t)$ was sampled intermittently at some fixed moments of time t^n and at discrete spatial locations x_i. Then, this discretized shape was transformed, through the scaling introduced in Equation (5.2b), to the profile $H(x,\tau)$. Based on self-similarity analysis, it is expected that the experimental shape function H plotted against ξ/ξ_N should agree well with the second-kind self-similar profile computed from the ODE in Equation (5.6). This agreement is, of course, contingent upon the gravity current having forgotten its initial condition. As discussed below, the memory of the IC plays a significant role in the pre-closure regime. Here, it is thus hypothesized that there exists yet another time scale, $t_{\text{sim}}(< t_c)$ after which the current has forgotten its IC and has 'truly' entered into the pre-closure self-similar regime. This hypothesis is substanti-

ated below, using numerical simulations performed via the proposed finite-difference scheme, which are compared to the experimental results.

5.4 Numerical Study of Pre- and Post-closure Self-similarity

To supplement the above mathematical analysis and the prior experimental study discussed, numerical simulations are now undertaken. The simulations allow for the closure time t_c and the time t_{sim} at which self-similarity sets in to be calcuated with some degree of confidence.

5.4.1 Pre-closure Self-similarity Analysis

From the discussion in Section 5.2 (see also [3, 38, 51]), it is expected that in second-kind self-similarity, $x_f(t)/x_f(0) \propto (\tau/t_c)^\delta$. From this expectation it follow that (now replacing $x_f(0)$ with x_0):

$$\frac{x_f(t)}{x_0} = b\left(\frac{\tau}{t_c}\right)^\delta \implies \frac{x_f(t)}{\tau^\delta} = \frac{bx_0}{t_c^\delta}. \tag{5.9}$$

Here, b is a 'pre-factor', which must be obtained from numerical simulations and/or experiments that are accurate enough to determine whether the current has entered in the self-similar regime. Since $\xi_N = x_f/\tau^\delta$ by definition, it follows that

$$\xi_N = \frac{bx_0}{t_c^\delta}, \tag{5.10}$$

where all terms on the right hand side are constant, restating the assumption in the self-similarity analysis that the similarity variable ξ maintains the constant value ξ_N at the current's front. It then follows that, during the initial adjustment from the initial condition, Equation (5.10) would not hold true. However, by $t = t_{\text{sim}}$ (to be determined numerically), the adjustment would be complete, allowing for the pre-factor b to be determined as the slope of the planar curve corresponding to plotting $x_f(t)/x_0$ versus $(\tau/t_c)^\delta$.

A numerical simulation for the experimental conditions described in Section 5.3 was performed. The IC should ideally correspond to the shape of the profile just after

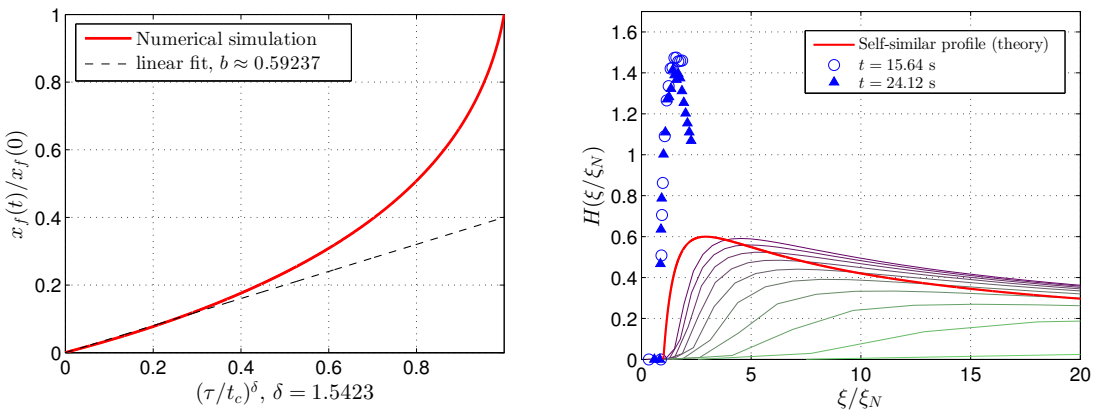

(a) (b)

Fig. 5.4. Numerical study of the pre-closure self-similar regime for a Newtonian gravity current ($r = 1$) in an HS cell with $n = 0.5$ ($\Rightarrow \delta \approx 1.5423$). Simulations were conducted based on experimental conditions (see Table 5.1) to (a) determine the time $t_{\text{sim}} \approx 43.55$ s required to forget the influence of IC (yielding pre-factor $b \approx 0.59237$), and (b) compare self-similar current shape profiles $H(\xi/\xi_N)$ between the predictions of mathematical analysis, numerical simulation and experiments. The pre-factor $b \approx 0.59237$ and closure time $t_c \approx 44.05$ s obtained from simulations were used to determine the value ξ_N. Experimental data was only available at $t = 15.6$ and 24.1 s. In (b), thin curves correspond to the profile from numerical simulations.

the lock-gate is opened. However, exact knowledge of this initial shape is difficult to obtain as the fluid shape adjusted quickly in the experiment. Instead, as a reasonable approximation, a 'boxy' polynomial was selected by setting $\gamma = 3$ in Equation (2.8) and using said profile as the IC $h(x, t = 0)$ for the simulations. While this choice may cause some deviation from the 'real' experimental conditions, the validity of this choice can be ascertained by verifying that the simulated value of t_c agrees well with the the experimental estimate. On the other hand, the choice of IC is expected to have an effect of on the value of t_{sim}, which represented time required for the IC to be forgotten.

The simulation was performed on the domain $x \in [0, L]$, where $L = 0.75$ m in accordance with the experimental setup. The domain was discretized into $N = 6001$

grid points. The simulation was run from $t_0 = 0$ s up to $t_f = 55$ s, over the course of $M = 5501$ time steps. The remaining parameters such the volume of the current, lock gate location, etc. were taken as specified in Table 5.1. The simulations yielded a closure time of $t_c = 44.05$ s, showing striking agreement with the experimental measurement. As shown in Figure 5.4a, the IC takes approximately $t_{\text{sim}} = 43.55$ s to be forgotten. This observation is made by following trend of the scaled nose position $x_f(t)/x_f(0)$ against the scaled time $(\tau/t_c)^\delta$. Requiring that these quantities become approximately linearly related, the threshold value t_{sim} was obtained. This numerical calculation yielded the pre-factor value of $b \approx 0.59237$.

Figure 5.4b shows the self-similar gravity current shape $H(\xi/\xi_N)$ as obtained from the mathematical analysis in Section 5.2, the numerical simulation of Equation (2.1) and experimental measurements. The universal self-similar profile was obtained by solving the ODE (5.6) using the procedure described in Section 5.2. The numerical profiles were obtained by scaling the solution to Equation (2.1) using the transformation in Equation (5.2b) in the time period $t \in [t_{\text{sim}}, t_c]$. While the analytical and numerical profiles show relatively good qualitative agreement, neither profiles agree with experimental data available at $t = 15.64$ and 24.12 s. It is thus concluded that the primary cause of this disagreement is the fact that the experimental data was recorded at times *much earlier* than onset of self-similarity at t_{sim}. Although it was expected that the experimental results would show agreement with self-similar profiles (from either phase-plane analysis or numerical simulation), the present discussion centering around t_{sim} suggests this would not be possible as the IC was not forgotten.

In closing, it is to be noted that, as $t \to t_c$ $(\tau \to 0^+)$, the self-similar behavior of the current rapidly breaks down as seen in Figure 5.4b, where the late-time green/light profiles lie appreciable far apart from the rest of the early-time purple/dark self-similar curves. This may indicate the existence of secondary self-similar regime, but this is beyond the scope of the present research. It would also be of interest to determine whether changing the HS cell geometry or initial lock-gate location might decrease t_{sim}. As it stands, for the experimental conditions detailed in Table 5.1, it is expected

the current is fully in the pre-closure self-similarity regime for the *extremely* short time period of $t \in [t_{\text{sim}}, t_c] \approx [43.55 \text{ s}, 44.05 \text{ s}]$.

5.4.2 Post-closure Self-similarity Analysis

The theory of the post-closure or leveling self-similar regime was firmly established in Section 5.2. However, unlike during pre-closure, the position of the current's front $x_f(t)$ is now fixed throughout the period of interest; specifically, it remains at the origin, i.e., $x_f(t > t_c) = 0$. This fact necessitates the replacement of $x_f(t)$ as a dynamic length scale. Therefore, the height of the current at the origin of the channel, $h(0,t)$, which is positive, is used as the dynamic length scale. Now, the self-similar behavior sought corresponded to integral curve connecting point D in the phase plane to point O (recall Figure 5.2). Here, the exact value of $U(\xi) = U_{\text{D}}$ is already known from solving the nonlinear eigenvalue problem in Section 5.2. Hence, substituting $u = (xU_{\text{D}})/\tau$ in Equation (5.1b), we obtain

$$\frac{\partial h}{\partial t} + \frac{1}{x^n}\frac{\partial}{\partial x}\left(x^n \frac{x}{\tau} U_{\text{D}} h\right) = 0 \implies \frac{\partial h}{\partial t} + \frac{U_{\text{D}}}{\tau}\left[\frac{1}{x^n}\frac{\partial}{\partial x}\left(x^{n+1}h\right)\right] = 0. \tag{5.11}$$

Changing variables from t to τ, and considering just the limiting behavior of the solution as $x \to 0^+$ (i.e., at the leveling point), Equation (5.11) becomes

$$\frac{\partial h}{\partial \tau} \approx \frac{U_{\text{D}}}{\tau}(n+1)h \implies h(0,\tau) \approx C|\tau|^{\kappa}, \tag{5.12}$$

where the exponent is $\kappa = (n+1)U_{\text{D}}$. The constant of integration, C must be obtained from numerical simulations. Introducing $h_\infty = \lim_{t\to\infty} h(0,t)$, it follows that $h(0,t)/h_\infty \propto (|\tau|/t_c)^{\kappa}$. Here, h_∞ represented the height of the current when leveling process is complete. Based on the mass conservation constraint, it is easy to show that

$$h_\infty = \frac{\int_0^L x^n h(x,0^+)\,\mathrm{d}x}{\int_0^L x^n\,\mathrm{d}x}. \tag{5.13}$$

In Equation (5.13), the numerator is equal to the total volume $\mathcal{V}_0$ of fluid released, and the denominator represents the cross-sectional area of the variable-width HS cell.

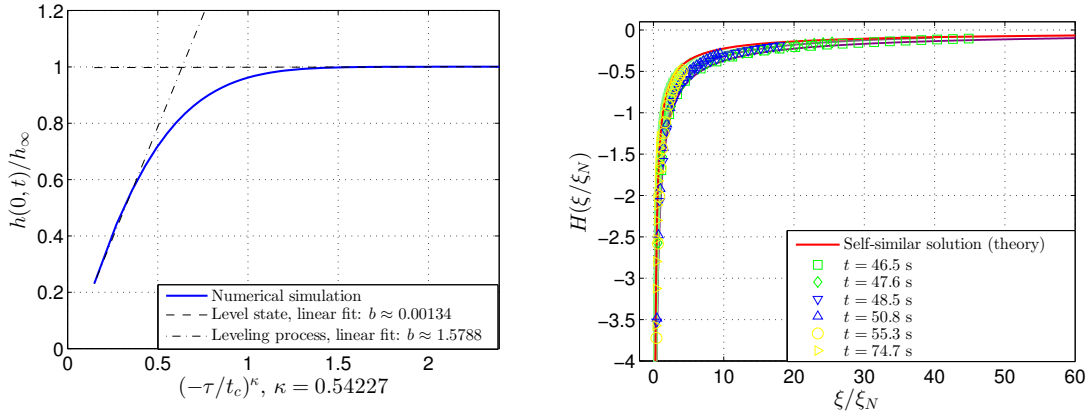

(a) (b)

Fig. 5.5. Numerical study of the post-closure self-similar regime for $n = 0.5$ ($\Rightarrow \delta = 1.5423$ and $U_\mathrm{D} = 0.36151$). Simulations were conducted based on the experimental conditions in Table 5.1 to (a) determine the pre-factor b during leveling of the current according to Equation (5.12) for $\kappa = 0.54227$, and (b) compare self-similar current shape profiles $H(\xi/\xi_N)$ between the predictions of mathematical analysis, numerical simulation and experiments. Asymptotically, a third pre-factor emerges during the final stages of the asymptotic leveling of the current profile, which is not used in the present study. The pre-factor $b \approx 1.5788$ was computed for the leveling behavior after the closure time $t_c \approx 44.05$ s (obtained in Section 5.4.1), from which the value of ξ_N was computed. Experimental data was only available at six moments of time in the post-closure regime.

A numerical simulation was performed over the spatial domain $x \in [0, L]$ where $L = 0.75$ m as before. The domain was discretized over $N = 3001$ points as discussed in Section 3.1. The simulation was advanced from $t_0 = 0$ s and up to $t_f = 270$ s. A closure time of $t_c \approx 44.05$ s was computed as mentioned earlier. The memory of the current's IC is not an issue in the post-closure self-similarity regime, as the self-similar process 'resets' after the current reaches the origin, and the pre-closure IC is thus irrelevant. Regardless, for completeness, it is to be noted that the IC for simulations was selected to be the same one as in the pre-closure study (Equation (2.8) with $\gamma = 3$). The remaining parameters were once again taken from Table 5.1.

The trend of scaled current height at the origin plotted against the scaled time in Figure 5.5a clearly indicates self-similarity as the current levels, yielding the pre-factor $b \approx 1.5788$. After some time, there is a transition from rising to an asymptotic adjustment as $h(0,t) \to h_\infty$. This latter regime is, however, a relatively straightforward observation, and it is not a topic of further interest here.

During the leveling period, excellent agreement is observed between the self-similar gravity current profiles, $H(\xi/\xi_N)$, obtained from mathematical analysis, numerical simulation and the experiment. The universal profile from theory established in Section 5.2 was derived by once again by solving the ODE system (5.6). The numerical profiles computed for $h(x,t)$ were scaled via the self-similarity transformation in Equation (5.2b). The experimental data comes from digitally sampling images of the profile $h(x,t)$ at six distinct times in the post-closure (i.e., $t > t_c$) regime.

In conclusion, the finite-difference numerical simulations of the full governing equation of the gravity current shape were extremely useful in ascertaining when the currents enters into the self-similar behavior described by the discussion in Section 5.2. Of particular use was the observation of the time t_{sim}, after which the current entered into pre-closure self-similarity. Obtain this result was easy once the simulation was performed, and there was no need to guesswork.

6. SUMMARY

In this thesis, a finite-difference numerical scheme for solving a family of nonlinear parabolic PDEs with variable coefficients given by Equation (2.1) is developed and benchmarked. A special feature of these nonlinear PDEs is that they possess solutions that can propagate in a wave-like manner with a finite speed of propagation. This study features an example from this family of PDEs for the one-dimensional spreading (propagation) of a power-law (Oswald–de Weale) fluid in a horizontal, narrow fracture with variable width. An emphasis is placed on designing a series of numerical tests that show conclusively that the proposed scheme is second-order accurate in space and time. Analytical self-similar solutions for special cases of the nonlinear parabolic PDE considered were used to benchmark the numerical method. Furthermore, the fact that a global mass conservation/injection constraint can be successfully reformulated into a set of nonlinear boundary conditions, which are implemented with second-order accuracy as well has been verified as well.

The main advantage of the finite-difference scheme discussed above is that it is strongly implicit, generalizing the time-stepping suggested by Crank and Nicolson [62]. Therefore, the proposed scheme does not formally require a time-step restriction for stability. By using a staggered grid, along the lines of Christov and Homsy [64], nonlinear terms can be handled within the same three-point stencil as the classical Crank–Nicolson scheme. This choice of grid is particularly convenient for the discretization of the nonlinear boundary conditions, allowing second-order accuracy to be achieved with just a two-point stencil near the domain boundaries. Using fractional steps in time ('internal iterations'), the nonlinear algebraic problem at each time step is reformulated as a fixed-point iteration.

Self-similar transformations have been shown to be a powerful tool for the analysis of viscous gravity currents. First-kind self-similar solutions can be obtained through

scaling analysis of the mathematical models, and often reduce the governing PDE to an exactly solvable ODE (in closed form), as summarized in Appendix A). In this thesis, first-kind exact solutions were used to benchmark the numerical method across a variety of flow problems. Consequently, the numerical simulations via the proposed scheme can now be used as a tool for exploring the *even further* self-similar behaviors.

Meanwhile, in flow regimes involving involving additional spatial (or temporal) scales, a scaling (dimensional) analysis is insufficient to reduce the governing PDE to a closed-form self-similar solution. Instead the problem requires, by phase-plane analysis techniques, deriving the self-similar transformation requires solving a nonlinear eigenvalue problem, as well as conducting numerical simulations (or experiments) to provide certain numerical constants that allow the second-kind self-similar transformation to be fully solved. Furthermore, in this case of second-kind self-similarity, numerical simulations are needed to even determine whether such flow regimes, predicted by mathematical theory, are actually manifested in reality. Second-kind self-similarity was explored in the context of the release of a fixed mass of Newtonian fluid spreading towards the origin of a horizontal, shaped HS cell of variable width. The self-similar transformation introduced, which involves the use of a self-similarity variable depending on the extra length (or time) scale, requires the computation of an unknown exponent δ, which is determined numerically as an eigenvalue. However, in the determining whether a given gravity profile $h(x,t)$ (found from either simulation or experiment) woill collapse on the predicted self-similar solution $H(\xi)$ (ξ being the similarity variable) obtained by second-kind self-similarity analysis, knowledge of the precise time period during which the current is expected to be in this self-similar regime is needed.

Previous work had not addressed the question of 'when' self-similarity begins, and it is indeed a difficult mathematical question in general. However, this time period that must elapse before the system is in a self-similar state can be directly determined by solving the governing PDE using the proposed numerical scheme. It turned out

that this period is exceptionally short during the pre-closure (spreading) regime of the gravity current, which leads to poor agreement with the experimental data, which is available at only two specific moments of time in the pre-closure regime. Nevertheless, numerical simulations were able to shed some light on this regime, specifically by conclusively showing the presence of two distinct self-similar regimes occurring during spreading and then during leveling. In the latter post-closure (leveling) stage of propagation, the gravity current shape profiles scaled via the second-kind self-similar transformation showed good agreement with mathematical predictions and experimental data.

7. RECOMMENDATIONS

7.1 Extensions of the Scheme to Incorporate Further Physical Effects

Owing to its accuracy and stability, the finite-difference scheme from [38], which was extended to non-Newtonian flows and benchmarked above, has been recently applied by Alhashim and Koch [74] to study hydraulic fracturing of low-permeability rock. This application is just one example of the potential utility of the proposed scheme in other fluid mechanics problems. In future work, an interesting extension to the proposed numerical scheme could be the inclusion of a generic source term of the form $\mathcal{S}(x,t,h)$, added to the right-hand side of Equation (2.1). Such a term can capture the effects of e.g., a leaky (porous) substrate over which a gravity current propagates, in which case $\mathcal{S}(x,t,h) = -\varkappa h(x,t)$ for some drainage constant $\varkappa$ [52,75] (see also [24, Section 9.2]). Then, the Crank–Nicolson disrectization in Equation (3.2) could be modified by adding

$$\frac{1}{2}\left[\mathcal{S}(x_i, t^{n+1}, h_i^{n+1}) + \mathcal{S}(x_i, t^n, h_i^n)\right] \tag{7.1}$$

to the right-hand side. Here, it is assumed that $\partial h/\partial x$ does not appear in $\mathcal{S}$ but only in $\mathcal{L}$. Therefore, the discretization in Equation (7.1) (even if nonlinear) will, at most, introduce a term in the matrix diagonal coefficient and a term on the right-hand side of Equation (3.9). Another variation on this theme involves the spreading of an unconfined viscous fluid above a deep porous medium into which it penetrates in a time-dependent manner over a depth of $l(x,t)$ [60]. Then, $\mathcal{S}(x,t,h) = -\kappa[1+h(x,t)/l(x,t)]$ and an additional ODE for $l(x,t)$ is coupled to Equation (2.1). This problem is an interesting avenue for future extension of the proposed scheme, as the ODE would have to be discretized for $l(x,t)$ in the same Crank–Nicolson sense as Equation (2.1) and add an extra equation (row) to the discrete problem in Equation (3.9).

On the other hand, an inclination angle (recall that all geometries in Figure 2.1 were lying flat, so gravity was directed in the $-y$-direction) results in a term proportional to $\partial h/\partial x$ being added to Equation (2.1) (for the case of a Newtonian fluid, see, e.g., [29,32]). This additional term changes the nonlinear diffusion equation (2.1) into a nonlinear *advection–diffusion* equation. Care must be taken in discretizing this new advective term. A similar PDE arises in the segregation of bidisperse granular mixtures [76, 77]. As discussed by Christov [78], a strongly implicit Crank–Nicolson scheme can be successfully used for these problems. The scheme in [78] is so robust that it performs well even in the singular vanishing-diffusivity limit of the advection-diffusion equation. Considering a generic advection term $\partial\Psi(h)/\partial x$, it can be handled analogously to the nonlinearity in the diffusion term. Specifically, we approximate

$$\left(\frac{\partial \Psi}{\partial x}\right)_{x=x_i} \approx \frac{1}{2}\left[\left(\frac{\Psi_{i+1}^{n+1}-\Psi_{i-1}^{n+1}}{2\Delta x}\right)+\left(\frac{\Psi_{i+1}^{n}-\Psi_{i-1}^{n}}{2\Delta x}\right)\right]. \tag{7.2}$$

Here, the advective term is discretized through a central difference formula involving a local three-point stencil on all interior nodes ($i = 1$ to $N - 1$). At the boundary nodes ($i = 0$ and $i = N$), one can use a three-point biased (forward or backward) difference formula, as described in Equations (3.8). The now well-established idea of staggering the nonlinear term across fractional time steps is carried forward (recall Equations (3.6)). However, to properly linearize the advective term within the internal iterations, it must be possible to write $\Psi(h) = \Upsilon(h)h$ (the most obvious way being $\Upsilon(h) \equiv \Psi(h)/h$) so that

$$\Psi_{i\pm1}^{n+1} \approx \Upsilon_{i\pm1}^{n+1/2,k} h_{i\pm1}^{n+1,k}. \tag{7.3}$$

Then, inserting Equation (7.3) into Equation (7.2) and adding the result to the left-hand side of Equation (3.9), modifies the tridiagonal system by adding $\Upsilon_{i\pm1}^{n+1/2,k}/(4\Delta x)$ to the superdiagonal $(i + 1)$ and subdiagonal $(i - 1)$. The remaining terms from Equation (7.2) are added to the right-hand side of the system.

Any of these potential extensions would have to be benchmarked against available first-kind self-similar solutions in [24, 29, 32, 60], however, no particular difficulties are expected to arise.

Another avenue of future work is as follows. Nowadays, high-order (i.e., greater than second-order) nonlinear parabolic PDEs are found to describe a wealth of low Reynolds number fluid phenomena: from the spreading and healing [72, 79] to the rupture dynamics [80] of thin liquid films dominated by capillary forces (see also [20, Ch. 6-C]). Typically, the spatial operator is of fourth order due to the inclusion of surface tension effects (which depend upon the curvature of the planar curve represented by $y = h(x,t)$), making the PDE more challenging to solve numerically. (Note that this is distinct from the inclusion of capillary effects in the context of gravity currents propagating in porous media described above, see [81].) Even higher (sixth) order thin film equations arise in dynamics of lubricated thin elastic membranes [82, 83] dominated by elastic forces. To interrogate these complex interfacial phenomena, there is a need for a robust and accurate numerical scheme to simulate these flows with low computational overhead (e.g., without the prohibitive time step stability restrictions of explicit schemes). In future work, it would be of interest to generalize the scheme from this chapter to such problems. Additionally, non-uniform (or adaptive) grids, which could be implemented along the lines of [66], can be used to capture singularity formation during thin film rupture.

7.2 Second-kind Self-similarity of Non-Newtonian Fluids

With respect to the numerical study of second-kind self-similarity, the obvious recommendation is to expand the analysis to the spreading and leveling of power-law non-Newtonian viscous gravity currents flowing towards the origin in a variable-width HS cell. It has been established that these kind of currents can be simulated with ease using the proposed scheme. For example, preliminary results suggest that, for the the case of a shear-thinning ($r = 0.5$) fluid in a HS cell having $n = 0.5$, the nonlinear eigenvalue problem can solved again to yield $\delta \approx 1.5836$, as determined by Longo [61]. However, it is expected that the phase-plane portrait for this case will possess rather different integral curves due to the appearance of $r \neq 1$ in the ODE

formulation of the second-kind self-similarity. Even though the integral curves will be different, the ODE nevertheless has the same critical points, immediately indicating existence of a pre- and post-closure self-similar regime for the non-Newtonian gravity current.

As a proof of concept, without the need for any special considerations, a numerical simulation was performed (with all parameters as in Table 5.1) to deduce the values of pre-factor slopes, t_{sim} and t_c for this a shear-thinning power-law fluid in a shaped HS cell ($r = n = 0.5$). The results are shown in Figure 7.1. The theoretical self-similar profile was obtained by solving the ODE system (5.7) between the appropriate critical points from Equations (5.8) via the shooting procedure described in Section 5.2 (and Appendix A). The clear presence of linear behavior in pre- and post-closure in Figures 7.1(a,b), respectively, supports the existence of two distinct self-similar regimes for power-law fluids, just as was the case for Newtonian fluids in Chapter 5. Thus, further experiments and simulations should be undertaken in the future to build upon and expand the understanding of this phenomenon. The most challenging aspect of future work, however, remains the issue of finding HS cell geometries and flow conditions that extend the range $[t_{\text{sim}}, t_c]$ to some non-trivial length, so that the pre-closure second-kind self-similar solution can be clearly observed.

In line with the above-proposed extension of the numerical scheme to a gravity current flow over a leaky substrate, numerical simulations of second-kind self-similar solutions of Newtonian and non-Newtonian flow over permeable surfaces can be undertaken. Based on the models in Tables 2.1 and 2.2, the current scheme can be used to complement the Newtonian-fluid studies of Zheng et al. [52] on two-dimensional axisymmetric gravity currents focusing towards an origin, flows towards the origin of shaped HS cells, or flows in horizontally heterogeneous porous media.

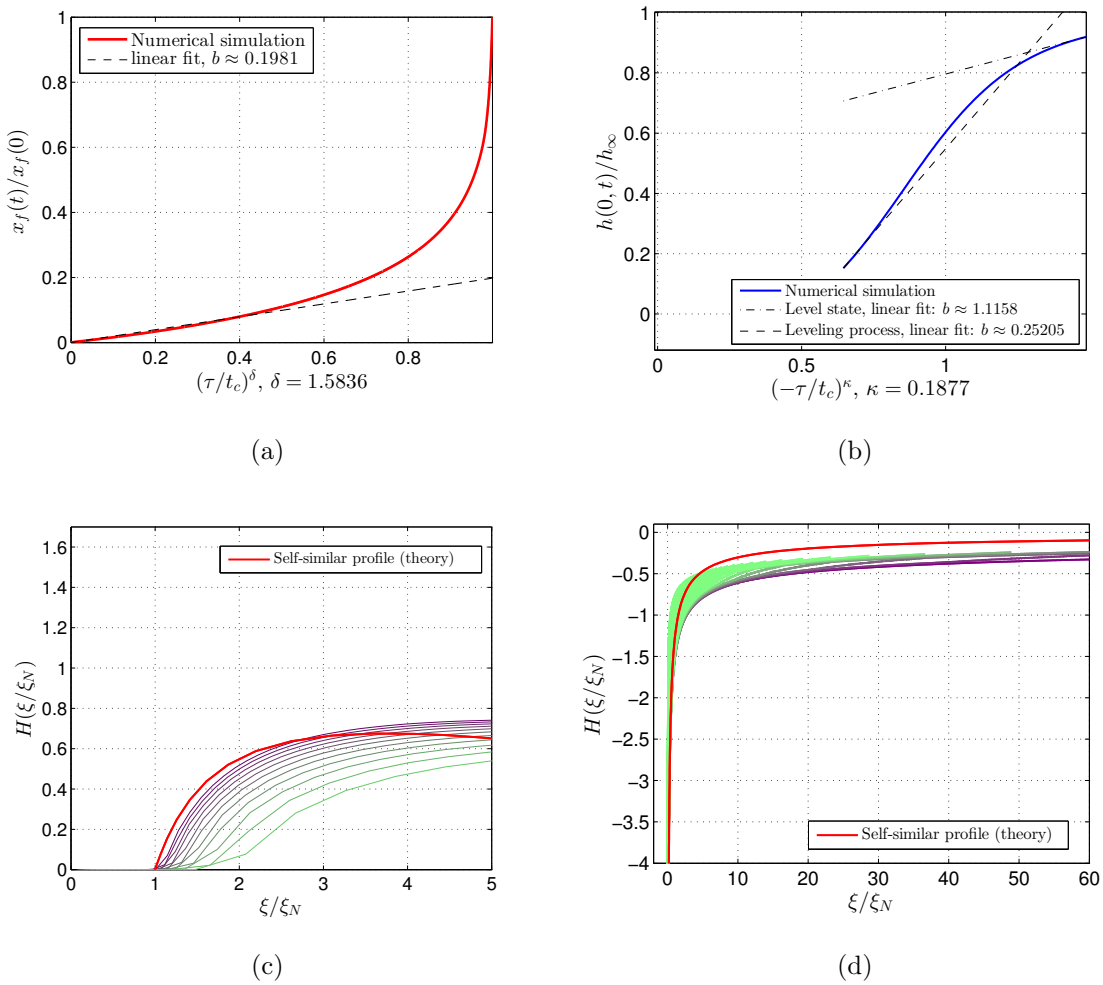

Fig. 7.1. Numerical study of second-kind self-similarity during the spreading and leveling of a power-law non-Newtonian fluid ($r = 0.5$) in a variable-width Hele-Shaw cell (shear-thinning, $n = 0.5$). Here, $\delta \approx 1.5836$ and $\kappa = (n+1)U_{\mathrm{D}} \approx 0.1877$. Simulations were performed on a domain $x \in [0, L]$, with $L = 0.75$ m and $N = 4501$ grid points. The profile was advanced from $t_0 = 0$ s to $t_f = 1100$ s through $M = 6501$ time steps. Experimental conditions in Table 5.1 were adopted. From simulations, pre-factors during (a) spreading $b \approx 0.1981$, and (b) during leveling $b \approx 0.25205$ were obtained. Additionally, it was found that pre-closure self-similarity emerges in $[t_{\mathrm{sim}}, t_c] \approx [120, 126.26]$ s after the IC was forgotten. Adopting dynamic scaling suggested by [61], there is a relatively good collapse of numerical profiles onto the universal theoretical solution derived from solving the ODE system (5.7), in both (c) pre-closure (spreading) and (d) post-closure (leveling).

REFERENCES

[1] A. Kolmogorov, I. Petrovskii, and N. Piskunov, "A study of the diffusion equation with increase in the amount of substance, and its application to a biological problem," in *Selected Works of A. N. Kolmogorov*, V. M. Tikhomirov, Ed. Dordrecht: Springer, 1991, pp. 248–270, translation of 1937 Russian original.

[2] R. A. Fisher, "The wave of advance of advantageous genes," *Ann. Eugenics*, vol. 7, pp. 353–369, 1937.

[3] G. I. Barenblatt, "On some unsteady fluid and gas motions in a porous medium (in Russian)," *Prikl. Mat. Mekh. (PMM)*, vol. 16, pp. 67–78, 1952.

[4] J. P. Ostriker, G. I. Barenblatt, and R. A. Sunyaev, Eds., *Selected Works of Yakov Borisovich Zeldovich*. Princeton, NJ: Princeton University Press, 1992, vol. 1.

[5] J. Engelbrecht, *Nonlinear Wave Dynamics: Complexity and Simplicity*. Dordrecht: Springer Science+Business Media, 1997.

[6] S. N. Vlasov and V. I. Talanov, "The parabolic equation in the theory of wave propagation," *Radiophys. Quantum Electron.*, vol. 38, pp. 1–12, 1995.

[7] W. Jerzak, M. D. Collins, R. B. Evans, J. F. Lingevitch, and W. L. Siegmann, "Parabolic equation techniques for seismic waves," *Pure Appl. Geophys.*, vol. 159, pp. 1681–1689, 2002.

[8] F. B. Jensen, W. A. Kuperman, M. B. Porter, and H. Schimdt, *Computational Ocean Acoustics*, 2nd ed. New York: Springer Science+Business Media, 2011.

[9] J. Engelbrecht, T. Peets, K. Tamm, M. Laasmaa, and M. Vendelin, "On the complexity of signal propagation in nerve fibres," *Proc. Estonian Acad. Sci.*, vol. 67, pp. 28–38, 2018.

[10] J. Engelbrecht, A. Salupere, A. Berezovski, T. Peets, and K. Tamm, "On nonlinear waves in media with complex properties," in *Generalized Models and Non-classical Approaches in Complex Materials 1*, H. Altenbach, J. Pouget, M. Rousseau, B. Collet, and T. Michelitsch, Eds. Cham, Switzerland: Springer International Publishing, 2018, pp. 248–270.

[11] C. I. Christov, G. A. Maugin, and A. V. Porubov, "On Boussinesq's paradigm in nonlinear wave propagation," *C. R. Mecanique*, vol. 335, pp. 521–535, 2007.

[12] L. C. Evans, *Partial Differential Equations*, 2nd ed. Providence, RI: American Mathematical Society, 2010.

[13] I. C. Christov, "Wave solutions," in *Encyclopedia of Thermal Stresses*, R. B. Hetnarski, Ed. Netherlands: Springer, 2014, pp. 6495–6506.

[14] Y. B. Zel'dovich and Y. P. Raizer, *Physics of Shock Waves and High-Temperature Hydrodynamic Phenomena*. Mineola, NY: Dover Publications, 2002, edited by W. D. Hayes and R. F. Probstein.

[15] B. Straughan, *Heat Waves*. New York, NY: Springer Science+Business Media, 2011.

[16] A. Berezovski and P. Ván, *Internal Variables in Thermoelasticity*. Cham, Switzerland: Springer International Publishing, 2017.

[17] B. H. Gilding and R. Kersner, *Travelling Waves in Nonlinear Diffusion-Convection Reaction*. Basel, Switzerland: Birkhäuser Verlag, 2004.

[18] J. L. Vázquez, *The Porous Medium Equation: Mathematical Theory*. Oxford, UK: Oxford University Press, 2007.

[19] H. E. Huppert, "The propagation of two-dimensional and axisymmetric viscous gravity currents over a rigid horizontal surface," *J. Fluid Mech.*, vol. 121, pp. 43–58, 1982.

[20] L. G. Leal, *Advanced Transport Phenomena: Fluid Mechanics and Convective Transport Processes*. New York: Cambridge University Press, 2007.

[21] N. Didden and T. Maxworthy, "Viscous spreading of plane and axisymmetric gravity waves," *J. Fluid Mech.*, vol. 121, pp. 27–42, 1982.

[22] G. I. Barenblatt and Y. B. Zel'dovich, "Self-similar solutions as intermediate asymptotics," *Annu. Rev. Fluid Mech.*, vol. 4, pp. 285–312, 1972.

[23] G. I. Barenblatt, *Similarity, Self-Similarity, and Intermediate Asymptotics*. Cambridge University Press, 1996.

[24] A. W. Woods, *Flow in Porous Rocks: Energy and Environmental Applications*. Cambridge, UK: Cambridge University Press, 2015.

[25] J. Bear, *Dynamics of Fluids in Porous Media*. Mineola, NY: Dover Publications, 1988.

[26] H. E. Huppert, "Geological fluid mechanics," in *Perspectives in Fluid Dynamics*, G. K. Batchelor, H. K. Moffatt, and M. G. Worster, Eds. Cambridge University Press, 2000, pp. 447–506.

[27] G. Felisa, A. Lenci, I. Lauriola, S. Longo, and V. D. Federico, "Flow of truncated power-law fluid in fracture channels of variable aperture," *Adv. Water Res.*, vol. 122, pp. 317–327, 2018.

[28] H. E. Huppert and J. A. Neufeld, "The fluid mechanics of carbon dioxide sequestration," *Annu. Rev. Fluid Mech.*, vol. 46, pp. 255–272, 2014.

[29] H. E. Huppert and A. W. Woods, "Gravity driven flows in porous layers," *J. Fluid Mech.*, vol. 292, pp. 55–69, 1995.

[30] D. M. Anderson, R. M. McLaughlin, and C. T. Miller, "The averaging of gravity currents in porous media," *Phys. Fluids*, vol. 15, pp. 2810–2829, 2003.

[31] S. Lyle, H. E. Huppert, M. Hallworth, M. Bickle, and A. Chadwick, "Axisymmetric gravity currents in a porous medium," *J. Fluid Mech.*, vol. 543, pp. 293–302, 2005.

[32] D. Vella and H. E. Huppert, "Gravity currents in a porous medium at an inclined plane," *J. Fluid Mech.*, vol. 555, pp. 353–362, 2006.

[33] M. A. Hesse, H. A. Tchelepi, B. J. Cantwell, and F. M. Orr Jr, "Gravity currents in horizontal porous layers: transition from early to late self-similarity," *J. Fluid Mech.*, vol. 577, pp. 363–383, 2007.

[34] D. M. Anderson, R. M. McLaughlin, and C. T. Miller, "A sharp-interface interpretation of a continuous density model for homogenization of gravity-driven flow in porous media," *Phys. D*, vol. 239, pp. 1855–1866, 2010.

[35] R. De Loubens and T. S. Ramakrishnan, "Analysis and computation of gravity-induced migration in porous media," *J. Fluid Mech.*, vol. 675, pp. 60–86, 2011.

[36] V. Ciriello, V. Di Federico, R. Archetti, and S. Longo, "Effect of variable permeability on the propagation of thin gravity currents in porous media," *Int. J. Non-linear Mech.*, vol. 57, pp. 168–175, 2013.

[37] H. E. Huppert, J. A. Neufeld, and C. Strandkvist, "The competition between gravity and flow focusing in two-layered porous media," *J. Fluid Mech.*, vol. 720, pp. 5–14, 2013.

[38] Z. Zheng, I. C. Christov, and H. A. Stone, "Influence of heterogeneity on second-kind self-similar solutions for viscous gravity currents," *J. Fluid Mech.*, vol. 747, pp. 218–246, 2014.

[39] R. B. Bird, R. C. Armstrong, and O. Hassager, *Dynamics of Polymeric Liquids*, 2nd ed. New York: John Wiley, 1987, vol. 1.

[40] V. Di Federico, S. Malavasi, and S. Cintoli, "Viscous spreading of non-Newtonian gravity currents on a plane," *Meccanica*, vol. 41, pp. 207–217, 2006.

[41] J. Gratton, S. M. Mahajan, and F. Minotti, "Theory of creeping gravity currents of a non-Newtonian liquid," *Phys. Rev. E*, vol. 60, pp. 6090–6097, 1999.

[42] C. A. Perazzo and J. Gratton, "Thin film of non-Newtonian fluid on an incline," *Phys. Rev. E*, vol. 67, p. 016307, 2003.

[43] L. Kondic, P. Palffy-Muhoray, and M. J. Shelley, "Models of non-Newtonian Hele-Shaw flow," *Phys. Rev. E*, vol. 54, pp. 4536–4539, 1996.

[44] L. Kondic, M. J. Shelley, and P. Palffy-Muhoray, "Non-Newtonian Hele-Shaw flow and the Saffman–Taylor instability," *Phys. Rev. Lett.*, vol. 80, pp. 1433–1436, 1998.

[45] G. Aronsson and U. Janfalk, "On Hele-Shaw flow of power-law fluids," *Eur. J. Appl. Math.*, vol. 3, pp. 343–366, 1992.

[46] I. Lauriola, G. Felisa, D. Petrolo, V. D. Federico, and S. Longo, "Porous gravity currents: Axisymmetric propagation in horizontally graded medium and a review of similarity solutions," *Adv. Water Res.*, vol. 115, pp. 136–150, 2018.

[47] C. A. Perazzo and J. Gratton, "Exact solutions for two-dimensional steady flows of a power-law liquid on an incline," *Phys. Fluids A*, vol. 17, p. 013102, 2005.

[48] V. Di Federico, R. Archetti, and S. Longo, "Similarity solutions for spreading of a two-dimensional non-Newtonian gravity current in a porous layer," *J. Non-Newtonian Fluid Mech.*, vol. 177-178, pp. 46–53, 2012.

[49] V. Di Federico, S. Longo, S. E. King, L. Chiapponi, D. Petrolo, and V. Ciriello, "Gravity-driven flow of Herschel–Bulkley fluid in a fracture and in a 2D porous medium," *J. Fluid Mech.*, vol. 821, pp. 59–84, 2017.

[50] V. Ciriello, S. Longo, L. Chiapponi, and D. Federico, "Porous gravity currents: A survey to determine the joint influence of fluid rheology and variations of medium properties," *Adv. Water Res.*, vol. 92, pp. 105–115, 2016.

[51] J. Gratton and F. Minotti, "Self-similar viscous gravity currents: phase plane formalism," *J. Fluid Mech.*, vol. 210, pp. 155–182, 1990.

[52] Z. Zheng, S. Shin, and H. A. Stone, "Converging gravity currents over a permeable substrate," *J. Fluid Mech.*, vol. 778, pp. 669–690, 2015.

[53] J. Gratton, "Similarity and self similarity in fluid dynamics," *Fund. Cosmic Phys.*, vol. 15, pp. 1–106, 1991.

[54] J. A. Diez, R. Gratton, and J. Gratton, "Self-similar solution of the second kind for a convergent viscous gravity current," *Phys. Fluids A*, vol. 6, pp. 1148–1155, 1992.

[55] S. B. Angenent and D. G. Aronson, "Intermediate asymptotics for convergent viscous gravity currents," *Phys. Fluids*, vol. 7, pp. 223–225, 1995.

[56] A. Oron, S. H. Davis, and S. G. Bankoff, "Long-scale evolution of thin liquid films," *Rev. Mod. Phys.*, vol. 69, pp. 931–980, 1997.

[57] J. Engelbrecht, *Questions About Elastic Waves.* Cham, Switzerland: Springer International Publishing, 2015.

[58] E. Boyko, M. Bercovici, and A. D. Gat, "Viscous-elastic dynamics of power-law fluids within an elastic cylinder," *Phys. Rev. Fluids*, vol. 2, p. 073301, 2017.

[59] R. T. Bonnecaze, H. E. Huppert, and J. R. Lister, "Particle-driven gravity currents," *J. Fluid Mech.*, vol. 250, pp. 339–369, 1993.

[60] J. M. Acton, H. E. Huppert, and M. G. Worster, "Two-dimensional viscous gravity currents flowing over a deep porous medium," *J. Fluid Mech.*, vol. 440, pp. 359–380, 2001.

[61] S. Longo, "Second-kind self-similar solutions for power-law and Herschel–Bulkley gravity currents," 2017, unpublished.

[62] J. Crank and P. Nicolson, "A practical method for numerical evaluation of solutions of partial differential equations of the heat-conduction type," *Math. Proc. Camb. Phil. Soc.*, vol. 43, pp. 50–67, 1947.

[63] J. Strikwerda, *Finite Difference Schemes and Partial Differential Equations*, 2nd ed. Society for Industrial and Applied Mathematics, 2004.

[64] C. I. Christov and G. M. Homsy, "Enhancement of transport from drops by steady and modulated electric fields," *Phys. Fluids*, vol. 21, p. 083102, 2009.

[65] N. N. Yanenko, *The Method of Fractional Steps.* Berlin/Heidelberg: Springer-Verlag, 1971, english translation edited by M. Hoult.

[66] C. I. Christov and K. Deng, "Numerical investigation of quenching for a nonlinear diffusion equation with a singular Neumann boundary condition," *Numer. Methods Partial Differential Eq.*, vol. 18, pp. 429–440, 2002.

[67] D. U. Von Rosenberg, *Methods for the Numerical Solution of Partial Differential Equations*, 3rd ed. New York: Elsevier, 1975.

[68] J. Douglas Jr., D. W. Peaceman, and H. H. Rachford Jr., "A method for calculating multi-dimensional immiscible displacement," *Petrol. Trans., AIME*, vol. 216, pp. 297–308, 1959.

[69] ——, "Numerical calculation of multidimensional miscible displacement," *Soc. Petrol. Eng. J.*, vol. 2, pp. 327–339, 1962.

[70] N. S. Cheng, "Formula for the viscosity of a glycerol-water mixture," *Ind. Eng. Chem. Res.*, vol. 47, pp. 3285–3288, 2008.

[71] A. Volk and C. Kähler, "Density model for aqueous glycerol solutions," *Exp. Fluids*, vol. 59, p. 75, 2018.

[72] Z. Zheng, M. Fontelos, S. Shin, and H. A. Stone, "Universality in the nonlinear leveling of capillary films," *Phys. Rev. Fluids*, vol. 3, p. 032001, 2018.

[73] L. I. Sedov, *Similarity and Dimensional Methods in Mechanics*, 10th ed. CRC Press, 1993.

[74] M. G. Alhashim and D. L. Koch, "The effects of fluid transport on the creation of a dense cluster of activated fractures in a porous medium," *J. Fluid Mech.*, vol. 847, pp. 286–328, 2018.

[75] D. Pritchard, A. W. Woods, and A. J. Hogg, "On the slow draining of a gravity current moving through a layered permeable medium," *J. Fluid Mech.*, vol. 444, pp. 23–47, 2001.

[76] V. N. Dolgunin and A. A. Ukolov, "Segregation modeling of particle rapid gravity flow," *Powder Technol.*, vol. 83, pp. 95–103, 1995.

[77] J. M. N. T. Gray, P. Gajjar, and P. Kokelaar, "Particle-size segregation in dense granular avalanches," *C. R. Phys.*, vol. 16, pp. 73–85, 2015.

[78] I. C. Christov, "On the numerical solution of a variable-coefficient Burgers equation arising in granular segregation," *Mat. Phys. Mech.*, vol. 35, pp. 21–27, 2018.

[79] Z. Zheng, M. Fontelos, S. Shin, M. D. Michael, D. Tseluiko, S. Kalliadasis, and H. A. Stone, "Healing capillary films," *J. Fluid Mech.*, vol. 838, pp. 404–434, 2018.

[80] V. Garg, P. M. Kamat, C. R. Anthony, S. S. Thete, and O. A. Basaran, "Self-similar rupture of thin films of power-law fluids on a substrate," *J. Fluid Mech.*, vol. 826, pp. 455–483, 2017.

[81] M. J. Golding, J. A. Neufeld, M. A. Hesse, and H. E. Huppert, "Two-phase gravity currents in porous media," *J. Fluid Mech.*, vol. 678, pp. 248–270, 2011.

[82] A. E. Hosoi and L. Mahadevan, "Peeling, healing, and bursting in a lubricated elastic sheet," *Phys. Rev. Lett.*, vol. 93, p. 137802, 2004.

[83] J. C. Flitton and J. R. King, "Moving-boundary and fixed-domain problems for a sixth-order thin-film equation," *Eur. J. Appl. Math.*, vol. 15, pp. 713–754, 2004.

A. FIRST-KIND SELF-SIMILAR SOLUTIONS FOR A POWER-LAW FLUID IN A SHAPED HELE-SHAW CELL

Viscous gravity currents exhibit self-similar propagation, meaning that the solution (at sufficiently 'long' times [23]) depends solely upon a combined variable of x and t, rather than on each independently. Self-similarity allows for the derivation of exact analytical solutions to the governing Equation (2.1) against which numerical solutions were benchmarked. Specifically, for the case of the release of a fixed mass of fluid ($\alpha = 0$ so that $\mathcal{V}(t) = \mathcal{V}_{\text{in}}\ \forall t \in [t_0, t_f]$), a closed-form analytical self-similar solution was used in Section 4.1 to test the order of convergence of the numerical scheme.

Following Di Federico et al. [49], the derivation of said self-similar solution for a power-law non-Newtonian fluid spreading *away* from the origin ($x = 0$) of a HS cell of uniform width b_1 ($n = 0$)[1] is summarized. First, the following dimensionless variables (with * superscripts) from [49] must be introduced:

$$x^* = \left(\frac{B}{A^\alpha}\right)^{1/(\alpha-2)} x, \qquad t^* = \left(\frac{B}{A^2}\right)^{1/(\alpha-2)} t,$$
$$h^*(x^*, t^*) = \left(\frac{B}{A^\alpha}\right)^{1/(\alpha-2)} h(x,t), \quad \text{(A.1)}$$

where A is the constant from Equation (2.1) (defined in Table 2.2) and $B = \mathcal{V}_{\text{in}}/b_1$. Hereafter, the * superscripts are dropped. Next, a suitable similarity variable η is selected. As discussed in Section 1, a self-similar solution of the first kind has the form $h(x,t) = t^\beta f(\eta)$ with $\eta = x/t^\delta$. Then, a scaling analysis of dimensionless version of Equation (2.1) yields

$$h(x,t) = \eta_N^{r+1} t^{F_2} f(\zeta), \qquad \eta = \frac{x}{t^{F_1}}, \qquad \zeta = \frac{\eta}{\eta_N}. \quad \text{(A.2)}$$

[1]While self-similar reductions are, of course, also possible for $n > 0$, they do not yield closed-form analytical solutions.

It can be shown that the constant η_N specifically corresponds to the value of η at the nose of the current, i.e., $\eta_N = x_f(t)/t^{F_1}$, where $x = x_f(t)$ is such that $h\big(x_f(t), t\big) = 0$. Here, ζ is a convenient rescaled similarity variable, and the exponents $F_{1,2}$ are

$$F_1 = \frac{\alpha + r}{r + 2}, \tag{A.3a}$$

$$F_2 = \alpha - F_1. \tag{A.3b}$$

The shape function $f(\zeta)$ represents the (universal) self-similar profile of the gravity current. This function is determined by substituting Equations (A.2) into the dimensionless version of Equation (2.1) to reduce the latter to a nonlinear ODE:

$$\frac{\mathrm{d}}{\mathrm{d}\zeta}\left(f\left|\frac{\mathrm{d}f}{\mathrm{d}\zeta}\right|^{1/r}\right) + F_2 f - F_1\zeta\frac{\mathrm{d}f}{\mathrm{d}\zeta} = 0, \qquad \zeta \in [0, 1]. \tag{A.4}$$

The second-order ODE in Equation (A.4) can be rewritten as a first-order system:

$$\frac{\mathrm{d}}{\mathrm{d}\zeta}\begin{Bmatrix} f_1 \\ f_2 \end{Bmatrix} = \begin{Bmatrix} f_2 \\ \dfrac{-r}{f_1 f_2 |f_2|^{(1-2r)/r}}\left(f_2|f_2|^{1/r} + F_2 f_1 - F_1\zeta f_2\right) \end{Bmatrix}, \tag{A.5}$$

where, for convenience, $f_1 = f$. The system in Equation (A.5) is 'stiff,' and requires use of an appropriate ODE solver, such as `ode15s` in MATLAB, subject to appropriate initial and/or boundary conditions at $\zeta = 0, 1$.

A peculiarity of this self-similar analysis is that only a single BC for the ODE (A.4) is known, namely $f(1) = 0$, i.e., this is the location of the gravity current's nose $x = x_f(t)$ at which $\zeta = \eta/\eta_N = 1$ and $h\big(x_f(t), t\big) = 0$. Since the ODE in Equation (A.5) requires a second initial or boundary condition, the 'backwards-shooting' idea introduced by Huppert [19] is used to provide a second condition near $\zeta = 1$. Then, the ODE in Equation (A.5) can be integrated 'backwards' from $\zeta = 1$ to $\zeta = 0$ subject to two 'initial' conditions at $\zeta = 1$.

To this end, consider the asymptotic behavior of the current near the nose. By assuming that $f \sim \mathfrak{c}_1(1 - \zeta)^{\mathfrak{c}_2}$ as $\zeta \to 1^-$ and substituting this expression into

Equation (A.4), $\mathfrak{c}_1 = F_2^r$ and $\mathfrak{c}_2 = 1$ is obtained by balancing the lowest-order terms. Now, two BCs are known (see also [49]):

$$f_1(1-\epsilon) = F_2^r \epsilon, \tag{A.6a}$$

$$f_2(1-\epsilon) = -F_2^r, \tag{A.6b}$$

for a sufficiently small $\epsilon \ll 1$. The system (A.5) can be solved subject to the 'final' conditions (A.6) on the interval $\zeta \in [0, 1-\epsilon]$. By convention, an ODE is solved with initial, not final, conditions. Therefore, the transformation $\zeta \mapsto 1 - \hat{\zeta}$ is performed, which leads to the right-hand-side of Equation (A.5) being multiplied by -1. Then, the final conditions in Equations (A.6) become initial conditions at $\hat{\zeta} = \epsilon$, and the first-oder system of ODEs is solved on the interval $\hat{\zeta} \in [\epsilon, 1]$.

For certain special cases, a closed-form analytical solution to Equation (A.4) can be obtained. For the case of the release of a fixed mass of fluid ($\alpha = 0$), Ciriello et al. [50] derived such an exact solution (can be verified by substitution):

$$f(\zeta) = \frac{r^r}{(r+2)^r (r+1)} \left(1 - \zeta^{r+1}\right), \tag{A.7}$$

which was used to benchmark the finite-difference scheme in Section 4.1. Finally, to obtain the viscous gravity current profile given in Equation (A.2) η_N must be computed. This value follows from imposing the mass conservation constraint in dimensionless form:

$$\eta_N = \left[\int_0^1 f(\zeta)\,\mathrm{d}\zeta\right]^{-1/(r+2)} \approx \left[\int_\epsilon^1 f(\hat{\zeta})\,\mathrm{d}\hat{\zeta}\right]^{-1/(r+2)}, \tag{A.8}$$

where the second (approximate) equality is needed for the case in which Equation (A.4) has to be integrated numerically (no exact solution); $\epsilon \ll 1$ is chosen sufficiently small.

Finally Equations (A.7) and (A.8) are combined and inserted into Equation (A.2), to analytically obtain the height profile over the fluid domain x at some time t. It should be noted, however, that for this solution to apply, the current must be in its self-similar regime, having forgotten any arbitrary initial condition from which it has evolved.